Inorganic Chemistry

Article

Cite This: Inorg. Chem. 2019, 58, 6199−6214

pubs.acs.org/IC

Enhanced Fe-Centered Redox Flexibility in Fe−Ti Heterobimetallic Complexes

James T. Moore,[†,#] Sudipta Chatterjee,[‡,#] Maxime Tarrago,[§,#] Laura J. Clouston,[†] Stephen Sproules,[⊥] Eckhard Bill,[∥] Varinia Bernales,[†] Laura Gagliardi,[†] Shengfa Ye,[*,§] Kyle M. Lancaster,[*,‡] and Connie C. Lu[*,†]

[†]Department of Chemistry, University of Minnesota, 207 Pleasant Street SE, Minneapolis, Minnesota 55455-0431, United States

[‡]Department of Chemistry and Chemical Biology, Baker Laboratory, Cornell University, Ithaca New York 14853, United States

[§]Max-Planck-Institut für Kohlenforschung, Kaiser-Wilhelm-Platz 1, 45470 Mülheim an der Ruhr, Germany

[∥]Max-Planck-Institut für Chemische Energiekonversion, Stiftstraße 34-36, 45470 Mülheim an der Ruhr, Germany

[⊥]WestCHEM, School of Chemistry, University of Glasgow, Glasgow G12 8QQ, United Kingdom

Supporting Information

ABSTRACT: Previously, we reported the synthesis of Ti[N(*o*-(NCH$_2$P(^{i}Pr)$_2$)C$_6$H$_4$)$_3$] and the Fe−Ti complex, FeTi[N(*o*-(NCH$_2$P(^{i}Pr)$_2$)C$_6$H$_4$)$_3$], abbreviated as TiL (**1**), and FeTiL (**2**), respectively. Herein, we describe the synthesis and characterization of the complete redox families of the monometallic Ti and Fe−Ti compounds. Cyclic voltammetry studies on FeTiL reveal both reduction and oxidation processes at −2.16 and −1.36 V (versus Fc/Fc$^+$), respectively. Two isostructural redox members, [FeTiL]$^+$ and [FeTiL]$^-$ (**2^{ox}** and **2^{red}**, respectively) were synthesized and characterized, along with BrFeTiL (**2-Br**) and the monometallic [TiL]$^+$ complex (**1^{ox}**). The solid-state structures of the [FeTiL]$^{+/0/-}$ series feature short metal−metal bonds, ranging from 1.94−2.38 Å, which are all shorter than the sum of the Ti and Fe single-bond metallic radii (cf. 2.49 Å). To elucidate the bonding and electronic structures, the complexes were characterized with a host of spectroscopic methods, including NMR, EPR, and ^{57}Fe Mössbauer, as well as Ti and Fe K-edge X-ray absorption spectroscopy (XAS). These studies, along with hybrid density functional theory (DFT) and time-dependent DFT calculations, suggest that the redox processes in the isostructural [FeTiL]$^{+,0,-}$ series are primarily Fe-based and that the polarized Fe−Ti π-bonds play a role in delocalizing some of the additional electron density from Fe to Ti (net 13%).

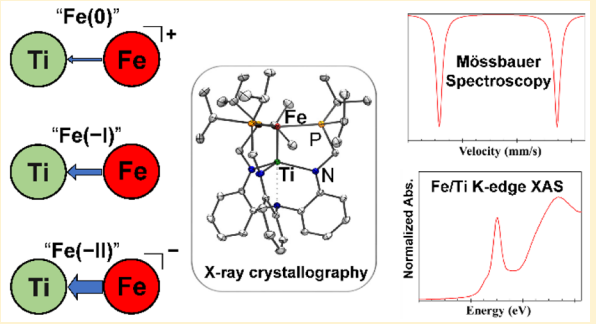

INTRODUCTION

Iron is ubiquitous in a variety of catalytic transformations in biology,[1−5] and is increasingly featured in synthetic processes as a viable alternative to toxic and/or precious metal catalysts.[6−10] For the oxygen-activating Fe enzymes that functionalize aliphatic C−H bonds, Fe^{IV}-oxo species are well established as key intermediates. The high-valent nature of the Fe oxo species and their synthetic models is supported by ^{57}Fe Mössbauer spectroscopy and synchrotron-based methods.[11,12] At the other extreme, subvalent Fe species also show utility in organic transformations. For example, [Li(TMEDA)]$_2$[Fe(C$_2$H$_4$)$_4$] is a precatalyst in cross-coupling reactions;[6,13,14] Collman's reagent, Na$_2$[Fe(CO)$_4$], is useful for a variety of organic transformations, including carbonylation, reductive coupling of two alkyl halides to form ketones, and the selective reduction of conjugated olefins.[7] In general, the isolation of these formally Fe^{-II} complexes requires strongly π-acidic ligands, with representative examples comprising 18-electron, homoleptic complexes supported by carbonyls,[15] isocyanides,[16−18] olefins,[19] and trifluorophosphines.[20] The spectroscopic, or physical, oxidation state of formally subvalent Fe compounds, however, remains largely unstudied. In one case, a detailed investigation of the [Fe(C$_5$Me$_5$)(η^4-anthracene)]$^{+/0/-}$ complexes revealed that the redox processes are primarily ligand-based and that the physical oxidation state remains Fe^{II}, thereby debunking the formal oxidation states of Fe^I and Fe^0 in this series.[21] Likewise, for Collman's reagent, an alternative interpretation of an Fe^{II} center with reduced CO ligands has been proposed.[22]

Another intriguing example of a formally subvalent Fe complex is [(TPB)Fe(N$_2$)]$^{2-}$, where TPB is tris(*o*-diisopropylphosphinophenyl)borane.[23] The physical oxidation state assignment is complicated by the delocalization of electron density via the Z-type Fe → B σ-bonding interaction, in addition to π-back-donation from Fe to the phosphines and N$_2$. The electronic configuration was represented by {FeB}^{10}, where the Feltham−Enemark notation[24] allows for the

Received: February 14, 2019
Published: April 8, 2019

DOI: 10.1021/acs.inorgchem.9b00442
Inorg. Chem. 2019, 58, 6199−6214

possibility of electron delocalization across the FeB unit and reflects the ambiguity in the oxidation states at Fe and B.[25−28]

We reasoned that formally subvalent Fe centers could also be stabilized via direct bonding to an electropositive transition metal. This strategy would leverage metal−metal covalency to enhance redox flexibility at the Fe center.[27,29−34] Specifically, the bonding between an early and late transition metal can be polarized to such an extent that the formal charges on the metals are zwitterionic. A notable example is (THF)Zr(μ-MesNP^{i}Pr$_2$)$_3$Co(N$_2$), whose electronic structure is consistent with that of a Co^{-I}Zr^{IV} core based on K-edge XAS data.[35] Currently, we extend this concept to FeTi complexes,[27,30,36] where the large electronegativity difference between Fe (1.80) and Ti (1.38) should also engender highly polarized Fe−Ti bonds where the electron density is mostly localized at Fe.[37−40]

Previously, TiL (**1**)[41] and FeTiL (**2**)[30] were reported, albeit with limited characterization data. Here, we report the full synthesis and characterization of **1**, **2**, and their isostructural redox counterparts. The [FeTiL]$^{+/0/-}$ series exhibits a large variation in the Fe−Ti bond length between each redox member. Hence, this series makes for an interesting study because of the complex interplay between electronic structure and chemical bonding. The ambiguity of the metal oxidation states can be constrained by considering two limiting extremes. By attributing the charge of the anionic donors solely to the bound metal, one would assign Ti^{III}, and hence Fe^{I}, Fe^{0}, and Fe^{-I}, in [FeTiL]$^{+/0/-}$, respectively. In contrast, the coordination chemistry of Ti is dominated by Ti^{IV}; thus, an alternative assignment is Fe^{0}, Fe^{-I}, and Fe^{-II}, respectively. To obtain insights into the underlying electronic structures, a host of physical and spectroscopic studies were conducted, including CV, EPR, ^{57}Fe Mössbauer, and multi K-edge XAS studies, as well as complementary DFT calculations.

RESULTS AND DISCUSSION

Electrochemical Characterization of FeTiL (2). The electrochemistry of complex **2** was probed using cyclic voltammetry (CV), as shown in Figures 1 and S1−S3.

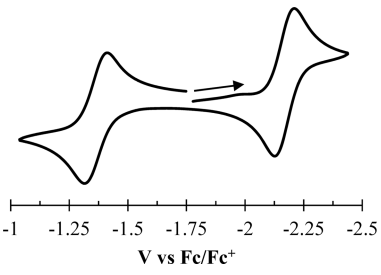

Figure 1. Cyclic voltammogram of **2** in 0.4 M [^{n}Bu$_4$N]PF$_6$ in THF at a scan rate of 50 mV/s. For additional CV studies of **2**, see Figures S1−S3.

Complex **2** features a reversible reduction process at −2.16 V versus Fc/Fc$^+$ (at 50 mV/s: i_{pa}/i_{pc} = 0.96, ΔE_p = 84 mV) and an oxidation event at −1.36 V (at 50 mV/s: i_{pc}/i_{pa} = 1.02, ΔE_p = 114 mV). As a comparison, the CV for the Ti monometallic complex, TiL (**1**), shows a Ti(III/IV) redox couple at −1.57 V (i_{pc}/i_{pa} = 0.93, ΔE_p = 174 mV at 50 mV/s, Figure S4).

To understand the nature of the redox processes in **2**, the redox potentials were compared to that of TiL (**1**) as well as to those of related Ti and/or bimetallic Fe−M complexes in the literature. Reports of Ti(III/IV) redox potentials are scarce, especially for complexes containing amido ligands. One example is the Ti^{IV} complex, Ti(κ^2-Me$_3$SiNCH$_2$CH$_2$NSiMe$_3$)$_2$,[42] for which the Ti(III/IV) potential is estimated to be −2.3 V versus Fc/Fc$^+$ based on the reported value of −1.91 V vs Ag/AgCl in THF.[43,44] By comparison, the Ti(III/IV) potential for **1** is 730 mV more positive. However, this large potential difference may be ascribed to the overall anionic charge and the greater number of amide donors for [Ti^{III}(Me$_3$SiNCH$_2$CH$_2$NSiMe$_3$)$_2$]$^-$ compared to **1**.

The oxidation process of **2** at −1.36 V is 210 mV more positive than that of **1**. Upon incorporation of the low-valent Fe metal into **1**, one might expect any localized Ti(III/IV) potential in the resulting bimetallic **2** to shift to more negative potentials compared to **1**, because of the additional electron density being donated from Fe to Ti. In support, the Ti(III/IV) oxidation for the isostructural NiTiL complex occurs at −1.90 V versus Fc/Fc$^+$ (Figure S5),[45] which is 330 mV *more negative* than that of **1**. Hence, we rule out the oxidation of **2** as being a Ti-centered redox process. We further propose that **2**^{ox} contains an Ti^{IV} center because an Fe^{0}Ti^{IV} assignment seems more reasonable than Fe^{I}Ti^{III}. The case of **2** remains unclear because the **2**^{ox}/**2** redox process can be either Fe-centered, e.g., Fe(0/−I), or delocalized across both transition metals, e.g., Fe(0)Ti(IV)/Fe(0.5)Ti(3.5).

The reduction process of **2** at −2.16 V versus Fc/Fc$^+$ may also be considered along two limiting scenarios, where the reduction is centered on either metal, i.e., Ti(IV/III) or Fe(−I/−II). While the former may appear more plausible, the latter cannot be fully ruled out. One analogue close to **2** that has also been investigated by CV is (TPB)Fe(N$_2$), which undergoes two reductions at −2.2 and −3.2 V versus Fc/Fc$^+$.[23] The second reduction process, which corresponds to {FeB}^{10}, is exceedingly more negative than that observed for {FeTi}^{10}, **2**^{red}. However, one caveat is that {FeB}^{10} is dianionic, whereas **2**^{red} is monoanionic. Moreover, direct comparisons to (TPB)Fe(N$_2$) may have limited utility since the Fe → B dative bond is quite distinct from the multiply bonded Fe≡Ti complexes (*vide infra*). Another relevant analogue is the N$_2$-labile Co alumatrane complex, (N$_2$)CoAlL, for which the "naked" [CoAlL]$^{0/-}$ reduction potential was measured at −2.10 V versus Fc/Fc$^+$ under Ar.[46] This redox potential, which has a similar value to that of **2**/**2**^{red}, was assigned as a localized d^9 Co^0/d^{10} Co^{-I} redox couple based on quantum chemical calculations.

Two other Fe−Ti systems have been reported in the literature: Ti(μ-XylNP^{i}Pr$_2$)$_3$FeBr[27] and Ti(μ-NP)$_3$Fe/K$_2$[(κ^1-NP)Ti(μ-NP)$_2$Fe],[36] where Xyl is xylyl and NP is diphenylphosphinopyrrolide. Unfortunately, no CV data for these complexes were reported. However, we can draw comparisons to the isostructural FeVL and FeCrL complexes, which show [FeML]$^{0/-}$ reduction potentials at −2.85 and −2.33 V, respectively. Intriguingly, the reduction potentials of the [FeML]$^{0/-}$ series, where M = Ti, V, and Cr, defy any periodic trend with respect to M because the potentials increase according to the order M = V ≪ Cr < Ti. Our best explanation, so far, is that the redox potentials are strongly tied to the total d−d electron valence count, where counts of 10, i.e., {FeM}^{10}, are strongly favored in these multiply bonded [FeML]^n complexes. The energetic preference for d−d counts of 10 is sensible because it would correspond to an electronic configuration of $(\sigma)^2(2\pi)^4(d_{x^2-y^2}, d_{xy})^4$,[29,31,32,47,48] which maximizes the population of bonding and nonbonding

DOI: 10.1021/acs.inorgchem.9b00442
Inorg. Chem. 2019, 58, 6199−6214

Scheme 1. Synthetic Routes to Ti Monometallic Compounds (1, 1^{ox}) and Bimetallic Fe–Ti Complexes (2, 2^{red}, 2-Br, and 2^{ox})

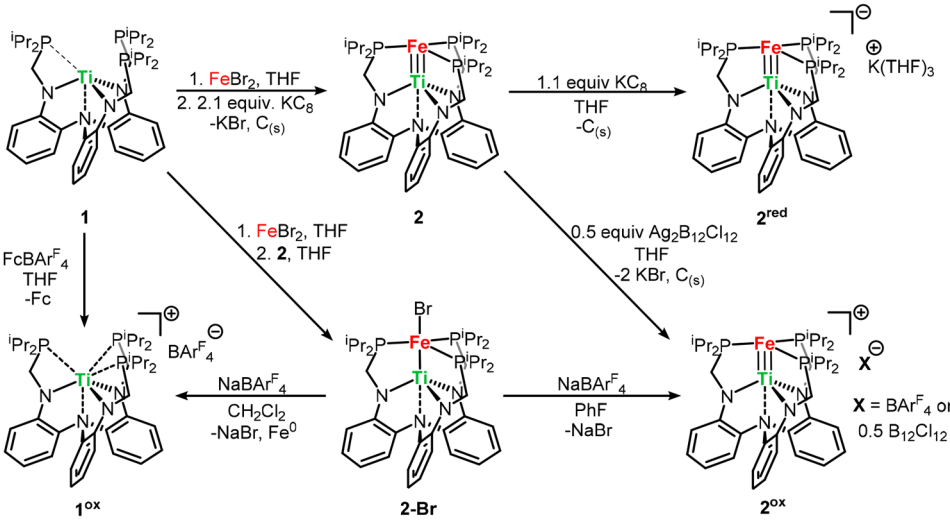

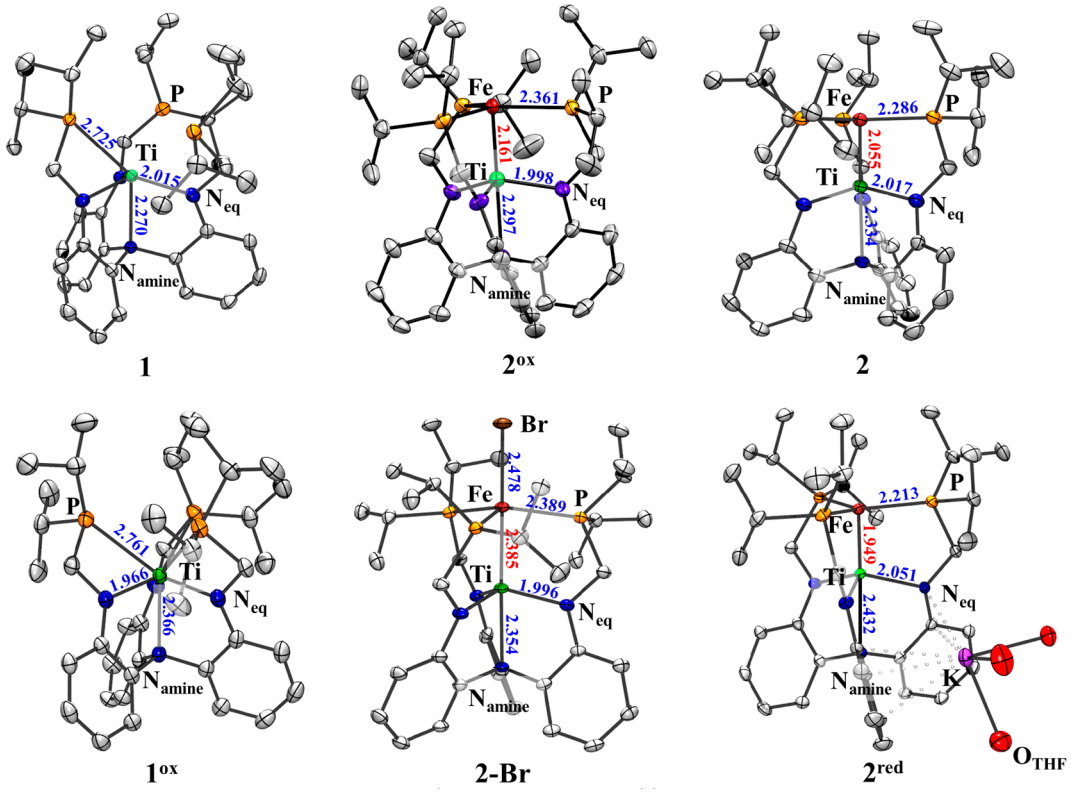

Figure 2. Solid-state structures of $[TiL]^{0/+}$ (**1**, $\mathbf{1}^{ox}$), $[FeTiL]^{-/0/+}$ ($\mathbf{2}^{red}$, **2**, $\mathbf{2}^{ox}$), and BrFeTiL (**2-Br**). Thermal ellipsoids are shown at 50% probability. Hydrogen atoms, noncoordinating solvents, and counterions are omitted for clarity. Titanium, green; iron, brick-red; phosphorus, orange; nitrogen, blue; and bromine, brown. The Ti–Fe bond distances (Å) are shown in red, while Ti–N (avg), Ti–N_{amine}, Fe–P (avg), and Fe–Br bond distances are shown in blue.

molecular orbitals. Hence, the $\mathbf{2}/\mathbf{2}^{red}$ reduction potential is the most mild because it favorably generates $\{FeTi\}^{10}$, whereas the corresponding $[FeVL]^{0/-}$ reduction potential is the most harsh because generating $\{FeV\}^{11}$ from $\{FeV\}^{10}$ is comparatively less favorable.

Synthesis of FeTiL Redox Series. The synthesis of the all redox members of the FeTiL family is shown in Scheme 1. As previously reported, complex **2** was prepared by mixing TiL (**1**), $FeBr_2$, and 2.1 equiv of the reductant, KC_8, in THF. Adding an additional equiv of KC_8 to **2** led to the further reduced member, $[FeTiL]^-$, which was isolated as K-$(THF)_3[\mathbf{2}^{red}]$. This synthetic route is preferred over the more direct reaction between $FeBr_2$, **1**, and 3 equiv KC_8 because it avoids having to separate $\mathbf{2}^{red}$ from the KBr byproduct. In contrast, the synthesis of $[FeTiL]^+$ ($\mathbf{2}^{ox}$) was less straightforward. Direct oxidation of **2** using $[Fc]BAr^F{}_4$ gave the desired product and a diamagnetic side product, which was independently identified as the monometallic complex, [TiL]-$BAr^F{}_4$, or $[\mathbf{1}^{ox}]BAr^F{}_4$, where Ar^F = 3,5-$(CF_3)_2$-C_6H_3. An improved synthesis of $\mathbf{2}^{ox}$ was devised that involved the

DOI: 10.1021/acs.inorgchem.9b00442
Inorg. Chem. 2019, 58, 6199–6214

Table 1. Selected Bond Lengths (Å), Bond Angles (deg), and Other Relevant Metrics for $[TiL]^{0/+}$ (**1**, $\mathbf{1}^{ox}$) $[FeTiL]^{-/0/+}$ ($\mathbf{2}^{red}$, **2**, $\mathbf{2}^{ox}$), and BrFeTiL (**2-Br**)

	1	1^{ox}	2^{red}	2[a]		2^{ox}	2-Br
Ti−Fe	N/A	N/A	1.9494(6)	2.0635(6)	2.0458(8)	2.1613(10)	2.3853(4)
FSR	N/A	N/A	0.78	0.83	0.82	0.87	0.96
d count	1	0	10	9		8	8
Fe−P[b]	N/A	N/A	2.2134(9)	2.2872(14)	2.2856(16)	2.3609(10)	2.3888(10)
Fe to P_3 plane	N/A	N/A	−0.1431(6)	−0.0373(5)	0.0208(7)	0.1429(9)	0.3578(4)
Ti−N_{eq}[b]	2.0149(25)	1.9663(7)	2.051(3)	2.016(3)	2.019(5)	1.998(3)	1.9956(27)
Ti to N_3 plane	0.4743(8)	0.5580(15)	0.5231(15)	0.4677(13)	0.4568(15)	0.4504(24)	0.4888(9)
Ti−N_{amine}	2.2697(13)	2.366(2)	2.423(3)	2.340(2)	2.328(2)	2.297(4)	2.3537(15)
Ti−P	2.7252(5)	2.7609(12)[b]	N/A	N/A	N/A	N/A	N/A
	N/A	N/A	118.67(3)	115.52(3)	117.21(4)	119.637(5)	117.65(2)
P−Fe−P	N/A	N/A	120.03(3)	127.84(4)	128.98(4)	119.637(5)	119.55(2)
	N/A	N/A	120.06(3)	116.57(4)	113.79(4)	119.637(5)	116.19(2)
Fe−Ti−N_{amine}	N/A	N/A	179.33(7)	178.40(7)	179.45(7)	180	178.69(4)
	115.73(6)	112.49(10)	107.95(10)	114.12(11)	112.73(12)	115.07(5)	114.35(7)
N_{eq}−Ti−N_{eq}	113.54(6)	111.31(10)	116.92(10)	114.38(11)	117.99(12)	115.07(5)	113.45(7)
	114.64(6)	113.04(10)	116.23(10)	115.86(11)	114.40(12)	115.07(5)	114.82(6)

[a]Two molecules in the asymmetric unit. [b]Average of the three values.

intermediacy of BrFeTiL (**2-Br**). The latter can be isolated from a comproportionation of **2** and "Br_2FeTiL", which is generated in situ from mixing **1** and $FeBr_2$ in THF.[49,50] Next, attempts to abstract the bromide in **2-Br** using $NaBAr^F_4$ in CH_2Cl_2 failed to provide $\mathbf{2}^{ox}$, leading instead to pure $\mathbf{1}^{ox}$. By changing the solvent to fluorobenzene, $[\mathbf{2}^{ox}]BAr^F_4$ was generated cleanly; however, we were unable to grow diffraction-quality single crystals. Installation of the highly crystalline dodecachlorododecaborate dianion[51,52] ($B_{12}Cl_{12}^{2-}$) through oxidation of complex **2** using $Ag_2B_{12}Cl_{12}$ allowed for the isolation of crystalline $[\mathbf{2}^{ox}]_2B_{12}Cl_{12}$.

X-ray Crystallography. All redox members of the TiL and FeTiL series were characterized through single-crystal X-ray diffraction studies. The corresponding solid-state structures are shown in Figure 2, and relevant structural metrics are provided in Table 1 (for more bond lengths and angles, see Table S1). Additionally, the metrics for **2** are included for comparison. Comparing the structures of **1** and $\mathbf{1}^{ox}$, the Ti−N_{eq} bond lengths contract by ∼0.05 Å upon oxidation of the Ti^{III} center to Ti^{IV}, respectively. In addition, the Ti center moves farther above the N_3-plane toward the phosphine donors with concomitant elongation of the Ti−N_{amine} bond by 0.1 Å. Greater interaction of the Ti(IV) center with all three phosphine donors is observed in $\mathbf{1}^{ox}$ where the average Ti−P distance is 2.76 Å. However, only a single phosphine donor binds to the Ti^{III} center in **1** (Ti−P = 2.7252(5) Å), while the other two Ti−P distances exceed 3.0 Å.

In all the FeTi complexes, the Ti−Fe bond lengths are smaller than the sum of their single-bond metallic radii (2.489 Å),[53] suggesting a strong interaction between Ti and Fe in these complexes. The formal shortness ratio (FSR),[54] defined as the ratio of the measured intermetal distance to the sum of the metals' single-bond radii, is useful to compare metal−metal bonding interactions between different bimetallic complexes. Typically, FSR values ≪1 denote metal−metal multiple bonding. The FSR values are all below unity (0.96 to 0.78) and decrease in the following order: **2-Br** > $\mathbf{2}^{ox}$ > **2** > $\mathbf{2}^{red}$. With each successive reduction or increase in the total d−d count from 8 to 10, the Ti−Fe bond contracts. Another geometric ramification of the strengthening of the Ti−Fe bond is gleaned by comparing the distance of the Fe center to the P_3-plane, in which Fe is slightly above the plane in $\mathbf{2}^{ox}$, within the plane in **2** and below the P_3-plane in $\mathbf{2}^{red}$. Notably, $\mathbf{2}^{red}$ is among only a handful of first row heterometallic complexes with metal−metal bond lengths shorter than 2.0 Å.[55−63] The Ti−Fe bond length of 1.9494(6) Å in $\mathbf{2}^{red}$ is close to that of $K_2[(\kappa^1\text{-NP})Ti(\mu\text{-NP})_2Fe]$, which currently has the shortest Ti−Fe bond in a coordination complex of 1.9474(7) Å (Table S2).[36] Additionally, the FSR value of 0.78 for $\mathbf{2}^{red}$ is identical to that of the isostructural MnCrL complex, which formally contains a quintuply bonded Mn−Cr unit.[29,32]

In these complexes, the first coordination sphere of each metal was scrutinized to assess whether redox changes occur at Ti, Fe, or both metal sites. In the Fe−Ti bimetallic complexes, the Ti−N_{eq} bond length elongates in the order **2-Br** ≈ $\mathbf{2}^{ox}$ < **2** < $\mathbf{2}^{red}$. Additionally, the average Fe−P bond length contracts in the same order, with $\mathbf{2}^{red}$ possessing the shortest Fe−P bond distance in the series. In considering the isostructural complexes, the contraction of the Fe−P bond distances from $\mathbf{2}^{ox}$ to **2** to $\mathbf{2}^{red}$ is consistent with increasing Fe → P π-back-bonding upon reduction of the FeTi core. Interestingly, plotting both the average Ti−N_{eq} and Fe−P bond distances versus total valence electron count for each complex show excellent correlations (R^2 > 0.99; Figure S13−S14). However, the overall change in Fe−P bond distances is greater (Δ = 0.15 Å) than that of the Ti−N_{eq} bond distances (Δ = 0.05 Å), suggesting that Fe is perturbed to a larger extent than Ti upon reduction. We note that these bond length changes cannot be accounted for solely by the polarizability difference between P and N. For instance, the $[FeCrL]^{+/0/-}$ complexes show the opposite trend in that the Cr−N_{eq} bond lengths vary more significantly (Δ = 0.14 Å) than the Fe−P bonds (Δ = 0.02 Å) across the series.[29,64] Finally, close examination of the P−Fe−P bond angles in the solid-state structure of **2** shows a significant distortion from C_3-symmetry, with one P−Fe−P angle being much larger than the rest (∼128°). This suggests a Jahn−Teller distortion arising from an unpaired electron that is localized at Fe in what would have otherwise been a degenerate pair of orbitals (*vide infra*).

NMR and EPR Spectroscopy. Complexes $\mathbf{1}^{ox}$ and $\mathbf{2}^{red}$ are diamagnetic, and the remaining complexes are paramagnetic. The ^{1}H NMR spectra of $\mathbf{1}^{ox}$ and $\mathbf{2}^{red}$ each show a total of 11

DOI: 10.1021/acs.inorgchem.9b00442
Inorg. Chem. 2019, 58, 6199−6214

unique peaks for the ligand protons, including 4 aryl, 2 diastereotopic methylene, 1 methine, and 4 unique methyl protons. This is most consistent with the complex possessing C_3 symmetry in solution, as a fully "locked" C_3-symmetric complex would display a total of 12 resonances.[29] The ^{1}H NMR spectrum of **2**, with 12 unique resonances, is fully consistent with C_3 symmetry. In contrast, complexes **2-Br** and [**2**^{ox}]BAr$^F_4$ only show 7 and 5 paramagnetically shifted resonances (excluding BAr$^F_4$ protons), respectively. The fewer number of resonances may indicate an average C_{3v} symmetry, which results from the fast exchange between the two propeller orientations, or that some signals are no longer observable due to paramagnetic broadening. Using Evans's method, the solution magnetic moments of **2-Br** and [**2**^{ox}]BAr$^F_4$ were determined to be 2.97(7) and 2.99(8) μ_B, respectively, which are consistent with S = 1 ground states (cf. spin-only μ = 2.83 μ_B).

The S = 1/2 spin state of **2** was confirmed by X-band EPR spectroscopy. As shown in Figure 3, the EPR spectrum of **2** at

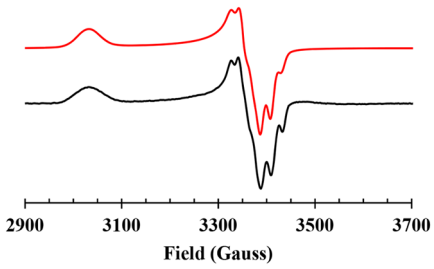

Figure 3. X-band EPR spectrum (9.65 GHz, 10 G, 6.33 μW) of **2** at 20 K in frozen toluene (1 mM). Experimental spectrum is shown in black, while the simulated spectrum is shown in red. Simulation parameters for **2**: g = (2.273, 2.051, 2.028), $A(3 \times {}^{31}P)$ = (24.0, 17.4, 21.0) × 10^{-4} cm^{-1} or (71.9, 52.2, 63.0) MHz. For alternative EPR simulations of this spectrum, see Figure S15.

20 K features a pseudo axial signal with g = (2.27, 2.05, 2.03), where the g_{avg} of 2.12 is greater than that of a free electron (g_e ≈ 2.002). Similar g-values were observed for the related {FeM}^{9} complexes: [(N$_2$)FeAlL]$^-$, (2.20, 2.04, 2.04); [FeVL]$^+$, (2.23, 2.08, 2.04); BrFeV(μ-^{i}Pr$_2$NPPh$_2$)$_3$, (2.13, 2.10, 2.06).[31,65,66] Additionally, a four-line hyperfine coupling pattern was discerned near $g_\perp$, which can be attributed to hyperfine coupling with three chemically equivalent ^{31}P (I = 1/2) nuclei, where $A_{avg}(^{31}P)$ is 62 MHz (for more simulation details, see Figures S15 and S16). Unfortunately, the ^{31}P hyperfine coupling interactions for the other {FeM}^{9} bimetallic compounds were not resolved by X-band EPR spectroscopy. The next best comparisons are [NiAlL]$^-$ and [NiGaL]$^-$, for which $A_{avg}(^{31}P)$ is 38 and 35 MHz, respectively.[67] Notably, the unpaired spin is delocalized across both the Ni and Al/Ga centers. Hence, the larger $A_{avg}(^{31}P)$ value for **2** is consistent with a localized Fe-based spin. As a control, the X-band EPR spectrum of **1** (Figure S17) shows an isotropic signal with g_{iso}= 1.95, which is consistent with other Ti^{III} complexes in the literature.[68−70] Overall, the $A_{avg}(^{31}P)$ value and the facts that $g_{avg} \gg g_e$ and $g_\parallel \gg g_\perp$, all indicate that the unpaired electron is localized in an Fe-based d orbital in the *xy*-plane.

DFT Calculations. Single-point hybrid density functional theory (DFT) calculations were carried out to elucidate the electronic structures of **2**^{ox}, **2**, and **2**^{red} (see the Experimental Section for details). The frontier molecular orbital (MO) diagrams are presented in Figure 4, and the corresponding orbital coefficients are given in Table 2. It should be noted that the selected MOs for **2**^{red} in Figure 4 are also representative of those for **2**^{ox} and **2**. Complete MO lists are available in Table S4 and Figure S19. All 3 complexes display polarized Fe−Ti bonding MOs, albeit with differing Ti contributions: two π-bonds (1e) comprising the Fe and Ti d_{xz}/d_{yz} orbitals and a σ-bond (1a$_1$) between the Fe and Ti d_{z2} orbitals. The Fe d_{xy} and d_{x2-y2} (2e) orbitals, however, are localized, precluding any Fe−Ti δ-bonds. Previously, polarized triple bonds were predicted for related heterobimetallic complexes, where bond polarization increases as the different metals' groups are further separated on the periodic table.[27,30,32] Also of interest is that the LUMO (2a$_1$) is similar across the series and has contributions from the Fe 4p, P 3s/3p, and Ti $3d_{z^2}$ orbitals. The Fe 4p and Ti $3d_{z2}$ contributions in the LUMO increase in the order of **2**^{red}, **2**, and **2**^{ox}, and hence are largest for the most oxidized Fe−Ti species, **2**^{ox}. The presence of an energetically low-lying metal-based p orbital has also been invoked in Ni^0 and Co^{-I} bimetallic complexes bearing a group 13 metalloligand.[71,72] In this work, the 2a$_1$ LUMO is important because it is the acceptor orbital for electronic transitions observed by Fe K-edge XAS in the pre-edge region (*vide infra*).

Complex **2**^{ox}, with an electronic configuration of $(1e)^4(1a_1)^2(2e)^2$, is best described as an Fe^0 center (S_{Fe} = 1) bound to a Ti^{IV} ion, due to the limited Ti participation in the 1e and 1a$_1$ MOs (13 and 15%, respectively). Upon reduction, the additional electron(s) are predicted to occupy the Fe d_{xy} and $d_{x^2-y^2}$ (2e) orbitals. Hence, the reduction to **2** and **2**^{red} may be viewed as Fe-centered reductions, resulting in electronic structures that approach Fe^{-I} and Fe^{-II}, respectively. The reduced Fe centers are likely stabilized by π-back-bonding to the phosphine moieties as well as increasingly covalent π-bonding with the Ti support. These effects can be observed in the increasing contributions of P in the 2e MOs (from 7% in **2**^{ox} to 19% in **2**^{red}), as well as Ti in the 1e MOs (from 13% in **2**^{ox} to 26% in **2**^{red}). The latter can be reasoned to manifest from (a) electrostatic attraction of Fe bearing negative charge to the electropositive Ti center as well as (b) improved energetic matching between atomic Ti and Fe 3d orbitals. These points are evidenced by the contraction of the Fe−Ti bond, which shortens by ∼0.1 Å per electron, and of the Fe−P bonds (∼0.07 Å per electron). As an aside, the presence of unequal number of electrons in the d_{xy} and $d_{x^2-y^2}$ orbitals of **2** leads to a Jahn−Teller distortion manifesting in unequal P−Fe−P angles and reflected in the nondegeneracy of the d_{xz}/d_{yz} and $d_{x^2-y^2}/d_{xy}$ pairs.

Mössbauer Spectroscopy. The FeTiL complexes were characterized by zero-field ^{57}Fe Mössbauer spectroscopy at 80 K (Figure 5). Notably, each reduction of the isostructural Fe−Ti complex is accompanied by a *decrease* in isomer shift (δ), where there is a reasonable correlation between the isomer shift and the total d−d count (R^2 = 0.95, Figure S22). The observed trend in the FeTiL series is also consistent with decreasing δ as the metal−metal interaction strengthens, i.e., decreasing FSR (R^2 = 0.96, Figure S23), which was previously noted by Thomas and co-workers for the Fe-M bimetallic families, where M is Nb, Ti, or V.[27,48,73] Surprisingly, the δ trend in the [FeTiL]$^{+/0/-}$ series is different from that observed for the isostructural FeVL and FeCrL series. For example, FeVL and [FeVL]$^+$ have identical isomer shifts, despite EPR evidence supporting an Fe-based redox change (Table S7; Figure S24).[31] For the FeCrL redox series, δ *increases* upon

DOI: 10.1021/acs.inorgchem.9b00442
Inorg. Chem. 2019, 58, 6199−6214

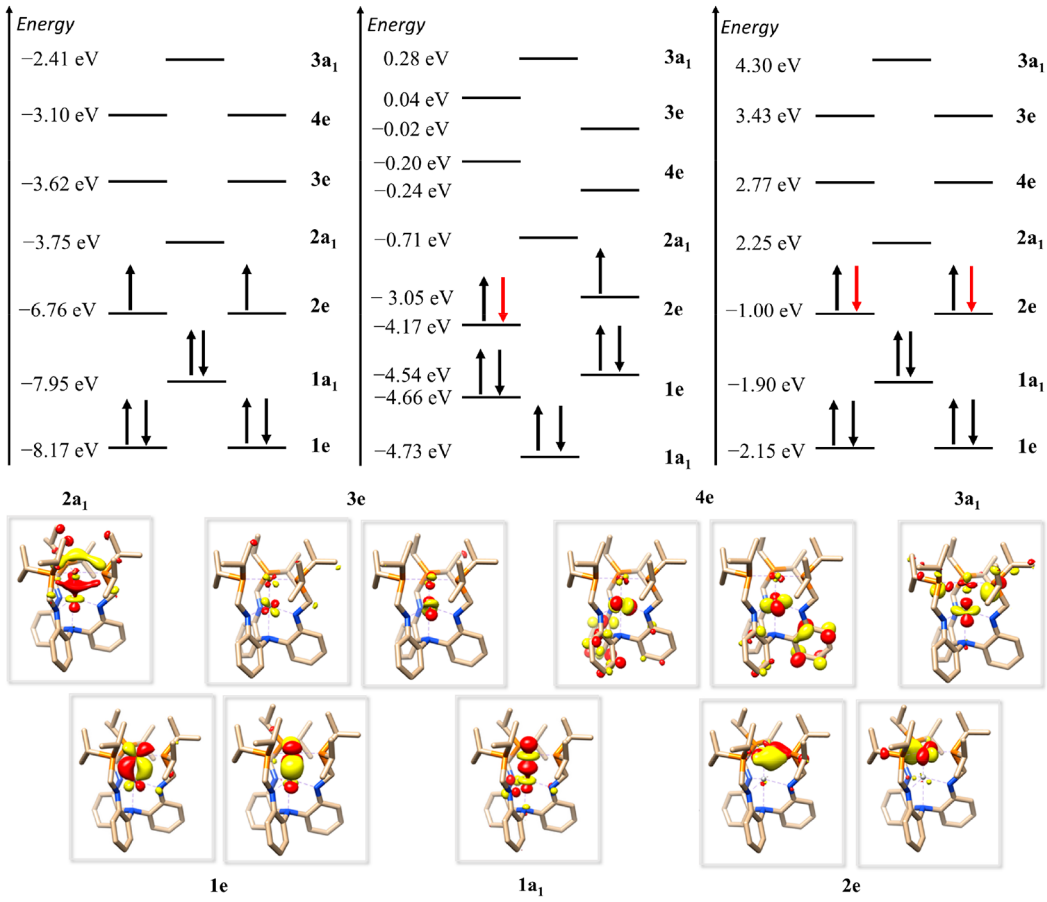

Figure 4. (Top) DFT-predicted electronic structures of $\mathbf{2}^{ox}$ (left), **2** (middle), and $\mathbf{2}^{red}$ (right). See Table 2 footnotes for computational details. (Bottom) Representative molecular orbitals from $\mathbf{2}^{red}$ represented by quasi-restricted orbitals.

Table 2. Molecular Orbital Composition Analyses for $\mathbf{2}^{ox}$, 2, and $\mathbf{2}^{red}$[a]

		$\mathbf{2}^{ox}$ (S = 1)				$\mathbf{2}^{b}$ (S = $^1/_2$)				$\mathbf{2}^{red}$ (S = 0)			
	orbital	% Fe 3d	% Fe 4p	% Ti 3d	% P[c]	% Fe 3d	% Fe 4p	% Ti 3d	% P[c]	% Fe 3d	% Fe 4p	% Ti 3d	% P[c]
1e	π ($d_{xz,yz}$)	76	0	**13**	3	65/66	1/1	**22/20**	6/7	58	1	**26**	8
$1a_1$	σ (d_{z2})	72	3	**15**	1	69	3	**17**	1	66	5	**19**	1
2e	Fe ($d_{x^2-y^2}$, d_{xy})	83	4	**0**	7	76/75	4/6	**2/0**	14/10	64	5	**3**	19
$2a_1$	LUMO	4	28	**13**	16	1	24	**9**	21	0	19	**9**	25

[a]Composition analysis = Löwdin population analysis. Single-point calculations were performed on structures (obtained from crystallographic coordinates where only the H atom positions were optimized; see the Experimental Section for details) at the B3LYP level of theory with the CP(PPP) basis set for Fe/Ti and def2-TZVP for all other atoms. The contribution of Ti 3d orbitals into bonding MOs are marked in bold. [b]Due to the Jahn−Teller distortion in **2**, "1e" and "2e" MOs are not degenerate. Hence, two values are given. [c]% P = sum of s, p, and d contributions from phosphorus.

reduction (Figure S25).[29,64] Also of relevance is that **2-Br** has a much higher isomer shift compared to the isoelectronic $[\mathbf{2}^{ox}]BAr^F_4$, which demonstrates the dramatic effect on δ that a differing coordination geometry can have. The δ of **2-Br** is reasonably close to that of Ti(μ-XylNP^{i}Pr$_2$)$_3$FeBr (c.f., 0.51 mm/s), which shares an identical primary coordination sphere around Fe.[27] Lastly, the isomer shift for **2** is identical to that observed in the $[(N_2)FeAlL]^-$ complex (δ = 0.38 mm/s), which was shown to possess an Fe^{-I} center.[66] It should be noted, however, that the presence of a π-acid (N_2) in $[(N_2)FeAlL]^-$ would also influence δ.

The magnitude of the quadrupole splitting parameter ($|\Delta E_Q|$) in the $[FeTiL]^{+/0/-}$ series increases with each successive reduction. Notably, this heterobimetallic series currently holds the largest variation in $|\Delta E_Q|$ across isostructural redox members, from a modest value of 0.79 mm/s for $\mathbf{2}^{ox}$ to a considerably large splitting of 4.32 mm/s for $\mathbf{2}^{red}$. To complicate matters, the isostructural Fe−Cr and Fe−V redox series consistently exhibit large quadrupole splitting (4.04 to 5.97 mm/s), whereas similar Fe−M bimetallic complexes supported by tris(phosphinoamido) ligands consistently display smaller $|\Delta E_Q|$ values (0.17 to 2.13 mm/s).[27,33,65] Thus, we turned to theory to gain a better understanding of how the electronic configurations of these bimetallic complexes influence the Mössbauer parameters.

^{57}Fe Isomer Shift. As tabulated in Table 3, the computed Mössbauer parameters (B3LYP; see the Experimental Section for details) show reasonable agreement with the experimental

DOI: 10.1021/acs.inorgchem.9b00442
Inorg. Chem. 2019, 58, 6199−6214

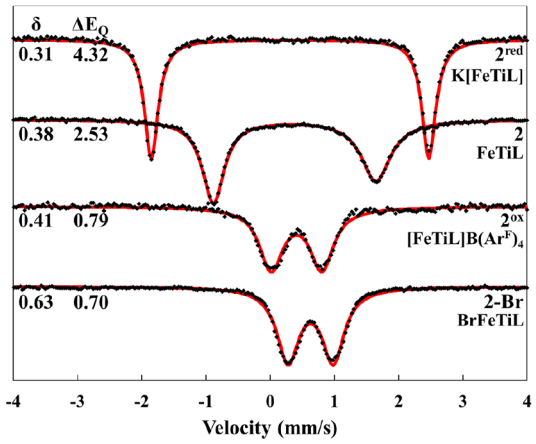

Figure 5. Zero-field ^{57}Fe Mössbauer spectra of the Fe−Ti bimetallic complexes at 80 K. Experimental data are shown using black dots, while the simulated spectra are shown in red. The asymmetry of the doublet from complex **2** was fit using a slightly different line-widths for each peak: 0.41 (left) and 0.56 (right) mm/s.

Table 3. Calculated Isomer Shifts (δ), Quadrupole Splittings (ΔE_Q), and Asymmetry Parameters (η) for 2^{ox}, 2, and 2^{red}

complex	δ (exp)	δ (calcd)	$\lvert\Delta E_Q\rvert$ (exp)	ΔE_Q (calcd)	η (calcd)
2^{red}	0.31	0.37	4.32	+3.61	0
2	0.38	0.41	2.53	+2.09	0.28
2^{ox}	0.41	0.44	0.79	+0.40	0

data. More excitingly, the computations reproduce the experimental trend that the isomer shifts of 2^{ox}, **2**, and 2^{red} decrease upon reduction, while $|\Delta E_Q|$ increases.

The ^{57}Fe isomer shift, which is proportional to the s electron density at the Fe nucleus (with an inverse relationship), has been shown to be most affected by changes in the valence 4s electron population.[74] The impact of an oxidation state change on the isomer shift can be understood by considering two primary effects, which have been classified as "electronic" and "geometric".[74] The electronic effect pertains to changes in the d count, where adding 3d electron(s) increasingly shields the 4s electrons, resulting in larger δ.[75,76] The geometric effect refers to structural perturbations, such as changes in metal−ligand bond lengths. For low-valent Fe complexes, contraction of metal−ligand bonds via π-back-bonding upon reduction lowers δ.[21,23,27,66,77,78] Hence, the electronic and geometric changes may exert opposing influences in low-valent Fe compounds, and their relative importance determines the directional change in δ.[79]

To better dissect the contribution of both factors, we devised two hypothetical molecules, **2*** and 2^{ox}*. These in silico complexes were generated by removing an electron from 2^{red} and **2**, respectively, and optimizing the wave function while constraining the molecular geometry. Hence, **2*** and 2^{ox}* have the d counts of **2** and 2^{ox}, respectively, but the geometry of 2^{red} and **2**, respectively. Following this method, the isomer shifts of **2*** and 2^{ox}* should reflect only the electronic impact of removing an electron. As shown in Figure 6, the electronic and geometric effects give rise to opposing trends in δ. More importantly, the geometric effect is dominant in the $[FeTiL]^{+/0/-}$ series, which rationalizes the observed trend of decreasing isomer shift upon reduction.

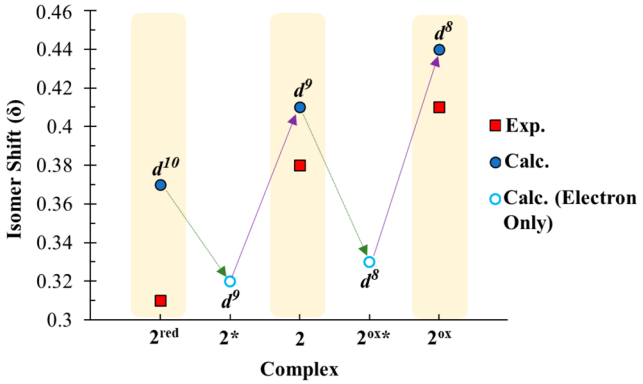

Figure 6. Calculated Mössbauer isomer shift after separate electron removal (green arrow) and subsequent geometric reorganization (purple arrow) steps. **2*** (δ = 0.32 mm/s) and 2^{ox}* (0.33 mm/s) are hypothetical complexes that are generated by removing an electron from 2^{red} and **2**, respectively. See the Experimental Section for details.

Quadrupole Splitting. The quadrupole splitting, ΔE_Q, reflects the interaction of the nonspherically distributed nuclear charge of the ^{57}Fe nuclear excited state (I = 3/2) with the surrounding electric field gradient (EFG). The quadrupole splitting is calculated according to the equation

$$\Delta E_Q = \frac{1}{2} eQV_{ZZ}\left(1 + \frac{\eta^2}{3}\right)^{1/2}$$

where eQ is the quadrupole moment of the iron nucleus, η is the asymmetry parameter such that $\eta = \frac{V_{XX} - V_{YY}}{V_{ZZ}}$, and V_{ii} are the eigenvalues of the EFG tensor at the nucleus. If the principal z-axis of the EFG tensor is colinear with a C_3 axis, then the equation simplifies to $\Delta E_Q = \frac{1}{2} eQV_{ZZ}$, since $V_{XX} = V_{YY}$ and η = 0. The trigonal symmetry of both 2^{ox} and 2^{red} motivates our focus on V_{ZZ} in elucidating the origin of both the anomalously large quadrupole splitting measured in 2^{red}, as well as the wide variation of $|\Delta E_Q|$ in the $[FeTiL]^{+/0/-}$ series (Table 3). Even in the case of **2**, which displays Jahn−Teller distortion, a calculated η value of 0.28 is still reasonably close to zero to allow for meaningful comparisons.

V_{ZZ} can be broken down into individual multicenter interactions that contribute significantly to the EFG at the Fe nucleus:[76,80]

$$V_{ZZ}^{total} = (V_{ZZ}^{1c,core} + V_{ZZ}^{1c,valence}) + (V_{ZZ}^{2c,bond} + V_{ZZ}^{2c,lattice}) + V_{ZZ}^{3c}$$

The first two terms represent one-center contributions to the EFG from Fe-based electrons, where one can separately consider the contributions of core (1s to 3p) and valence (3d) electrons. Smaller valence contributions to the EFG can also arise from the mixing of Fe orbitals into ligand-based MOs. The next pair of terms arise from two-center interactions with the ligand-based electrons. Again, one can segregate contributions from electrons that are directly bonded to Fe and those that act as point-charges, which are denoted as "lattice". The last term represents three-center contributions, which typically have a negligible impact on V_{ZZ}.

Table 4 summarizes the individual contributions of the V_{ZZ} for the $[FeTiL]^{+/0/-}$ series (for the orbitals used for these calculations, see Figures S27−S29). The DFT-calculated values

DOI: 10.1021/acs.inorgchem.9b00442
Inorg. Chem. 2019, 58, 6199−6214

Table 4. Computed V_{zz} Values (in a.u.) for 2^{ox}, 2, and 2^{red} and the Contributions from the Core and 3d Electrons

complex	$V_{ZZ}^{1c,core}$	$V_{ZZ}^{1c,valence}$	$V_{ZZ}^{2c,bond}$	$V_{ZZ}^{2c,lattice}$	V_{ZZ}^{3c}	V_{ZZ}^{total}
2^{ox}	0.84	−1.18	0.54	0.02	0.02	0.24
2	0.70	−0.04	0.57	0.01	0.03	1.27
2^{red}	0.62	0.60	0.94	0.02	0.03	2.21

indicate three dominant terms: $V_{ZZ}^{1c,core}$, $V_{ZZ}^{1c,valence}$, and $V_{ZZ}^{2c,bond}$. Interestingly, the $V_{ZZ}^{1c,core}$ terms for 2^{ox}, 2, and 2^{red} are found to be atypically large, with values ranging from 0.62−0.84 a.u. in this series. It should be noted that the polarization of core electrons is difficult to achieve and typically requires strong metal−ligand bonding, for instance, Fe^{IV}-oxo species.[80,81] Presumably, the presence of the Fe−Ti bonding is sufficient to induce distortion of the inner-shell electron density, which by proximity to the Fe nucleus, can result in a sizable EFG. To the best of our knowledge, the polarization of core electrons has never been elucidated in complexes featuring metal−metal multiple bonds. The $V_{ZZ}^{2c,bond}$ term, however, is expected to be significant for low-valent Fe complexes because metal−ligand bonds are typically short and covalent. For 2^{ox}, 2, and 2^{red}, this contribution is traced to the lone-pair electrons on the phosphine donors, which is reflected by the presence of Fe p_x, p_y, d_{xy} and $d_{x^2-y^2}$ character in the P-based σ-bonding orbitals. Lastly, the $V_{ZZ}^{1c,valence}$ term is intriguing because it is largely responsible for the variations in V_{ZZ}, and hence, ΔE_Q in this series. For the valence contributions, any charge that is localized perpendicular to V_{ZZ}, e.g., Fe d_{xy}, $d_{x^2-y^2}$, yields a positive contribution to V_{ZZ}, whereas any charge parallel to V_{ZZ}, e.g., Fe d_{xz}, d_{yz}, d_{z^2}, yields a negative contribution.[76] Throughout the redox series from 2^{ox} to 2 to 2^{red}, the Fe d_{xy} and $d_{x^2-y^2}$ orbitals become increasingly occupied. Hence, the most positive $V_{ZZ}^{1c,valence}$ contribution is predicted for 2^{red}, which is consistent with 2^{red} having the largest $|\Delta E_Q|$ in the series. Moreover, the $V_{ZZ}^{1c,valence}$ term could rationalize the consistently larger $|\Delta E_Q|$ values for the isostructural FeCr and FeV redox members, for which the Fe d_{xy} and $d_{x^2-y^2}$ orbitals are fully occupied in all but one case, $[FeVL]^+$.

XAS Studies. The Fe and Ti K-edge XAS for 2^{red}, 2, 2^{ox}, and **2-Br** (Figure 7a,b) were obtained to further unravel any ambiguities distinguishing their physical from their formal oxidation states. Because rising edge energies are often insufficient metrics of physical oxidation state,[82−84] the discussion mainly focuses on the pre-edge regions. Overall, the experimental metal K-edge pre-edge features are well-reproduced using time dependent DFT (TD-DFT) calculations (Figures 7c,d and S34−S43), serving as the basis for the interpretations provided below. The strong correlation (R^2 = 0.95 and 0.82 for Fe and Ti, respectively, Figure S30) between calculated and experimental pre-edge features affords confidence in using the underlying single point calculations to assign transitions from Fe or Ti 1s to particular acceptor MOs (to compare the results from these computational methods to those presented above, see Figure S20 and Table S5). These assignments are presented in Table 5 (Table S9 and Figures S44−S51).

The Fe K-edge XAS of 2^{red}, 2, and 2^{ox} all exhibit a well-resolved pre-edge absorption feature near 7112 eV (Figure 7a). Typically, pre-edge features in first-row transition metal K-edge XAS arise from quadrupole-allowed 1s → 3d excitations, which can gain intensity from 4p admixture, or from excitations to low-lying ligand-based MOs.[84−86] In the present case, the substantial Fe $4p_z$ character in the acceptor MO (LUMO $2a_1$, Figure 4) is responsible for the high intensity of the pre-edge peaks in 2^{red}, 2, and 2^{ox}. Notably, **2-Br**, which does not share this LUMO (Figure S21), lacks an intense pre-edge feature.

Importantly, for 2 and 2^{ox}, an additional transition was observed (and predicted) as a lower energy shoulder to the intense pre-edge peak, which is absent for 2^{red} (red trace,

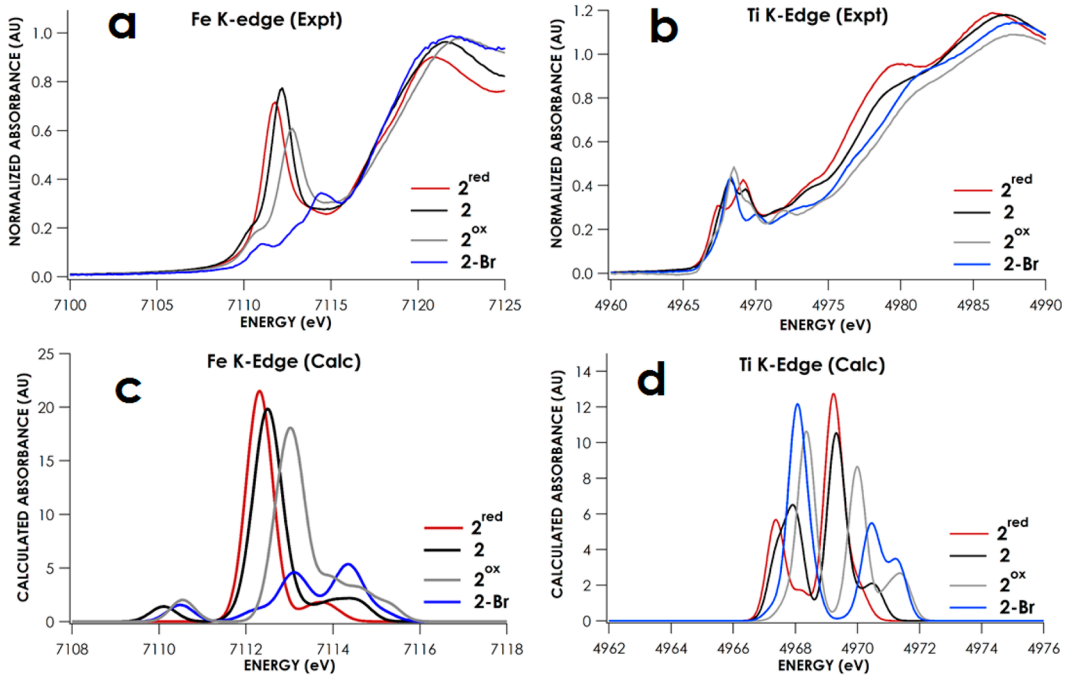

Figure 7. Overlaid K-edge spectra of Fe, (a) experimental and (c) TD-DFT calculated, and Ti, (b) experimental and (d) TD-DFT calculated, for complexes 2 (black), 2^{red} (red), 2^{ox} (gray), and **2-Br** (blue). All data were obtained on solid samples diluted in BN and maintained at 10 K.

DOI: 10.1021/acs.inorgchem.9b00442
Inorg. Chem. 2019, 58, 6199−6214

Table 5. Experimental Fe and Ti Pre-Edge Peak Energies and Peak Assignments for FeTi Redox Series[a]

	Fe pre-edge peak energy (eV)		Ti pre-edge peak energy (eV)	
transitions[b]	Fe 1s → $2a_1$	Fe 1s → 2e	Ti 1s → 3e/4e	Ti 1s → $2a_1$
$\mathbf{2}^{red}$	7111.8	N/A	4967.3	4969.1
2	7112.2	7110.1	4968.3	4969.3
$\mathbf{2}^{ox}$	7112.8	7110.6	4968.5	4969.7[c]
2-Br	7111.0;[d] 7113.1;[e] 7114.3[f]		4968.3[g]	

[a]For more detailed transition assignments, see Table S9. Pre-edge peak energies are obtained from the corresponding second derivative plots of the K-edge XAS spectrum. [b]Primary orbital contribution. [c]Transitions also include additional contributions from the MO $3a_1$. [d]Transitions also include additional contributions from the MOs 2e and 3e. [e]Transitions also include additional contributions from the MOs 3e and aromatic π^*. [f]Transitions also include additional contributions from the MO $3a_1$, 4e, and aromatic π^*. [g]Transitions also include additional contributions from the MOs $3a_1$, 3e, 4e, and aromatic π^*.

Figure 7a,c). This feature is assigned to the Fe 1s → 2e (Fe $3d_{x^2-y^2}$, $3d_{xy}$) transition. Moreover, its absence in $\mathbf{2}^{red}$ confirms the filling of Fe-localized valence vacancies present in **2** and $\mathbf{2}^{ox}$, which substantiates the hypothesis that the redox changes are Fe-based. In further support, the electronic absorption spectrum of $\mathbf{2}^{red}$ lacks any transitions at wavelengths longer than 900 nm, which suggests the absence of any d−d transitions, consistent with a fully filled valence shell. In contrast, both **2** and $\mathbf{2}^{ox}$ display band(s) in the near-infrared region that can plausibly be assigned as d−d transitions (Figure S18 and Table S3).

The Ti K-edge XAS data of $\mathbf{2}^{red}$, **2**, $\mathbf{2}^{ox}$ and **2-Br** (Figure 7b) all exhibit two main pre-edge features with similar intensities in the range 4967.3−4969.3 eV (Table 5). On the basis of TD-DFT, the lower energy feature in the Ti XAS of the isostructural FeTiL complexes is assigned as the Ti 1s → 3e/4e (Fe−Ti π^*/Ti $3d_{x^2-y^2}$, $3d_{xy}$) transition, while the higher energy feature is assigned as the Ti 1s → $2a_1$ (LUMO) transition. The latter feature allows a useful comparison to the Fe 1s → $2a_1$ transition because they both share a common primary acceptor orbital. Notably, the energy shift of the Fe 1s → $2a_1$ transition across the redox states (Δ = 1.0 eV) is greater than that of the corresponding Ti 1s → $2a_1$ transition (Δ = 0.6 eV). Of note, Thomas and co-workers have observed a similar 0.5 eV variation in the Zr K-edge energies of several heterobimetallic ZrCo complexes, for which the Zr^{IV} oxidation state is invariant and Co is the redox-active center.[35] Hence, the comparison of the energy shifts for the 1s → $2a_1$ excitations points to Fe as the redox active site.

One counterargument is that the first pre-edge feature in the Ti XANES of the isostructural redox series also has a sizable shift (Δ = 1.2 eV). However, these transitions are more complex in nature, involving multiple Ti 3d-based orbitals. Also, the plot of the pre-edge peak energies versus the total d electron count (Table S10, Figure S52) exhibits a strong linear correlation for both the Fe 1s → $2a_1$ and Ti 1s → $2a_1$ transition, with R^2 = 0.99 and 0.96, respectively. By contrast, a worse correlation (R^2 = 0.87) is found for the analogous plot of the Ti 1s → 3e/4e peak energies. At this time, we do not understand why the energies are more perturbed for the Ti 1s → 3e/4e peaks across the isostructural redox series. Lastly, the features in the Ti XANES of **2-Br** are even more complex in nature, involving multiple acceptor orbitals, including ligand-based π^*-MOs (see Tables 5 and S9).

SUMMARY AND CONCLUSIONS

A series of Fe−Ti bimetallic complexes was investigated to better understand the nature of polarized metal−metal bonding interactions between early and late first row transition metals. These Fe−Ti compounds add to a growing number of heterobimetallic complexes featuring short metal−metal bonds and a handful of complexes featuring direct Fe−Ti bonds. Collectively, the isostructural Fe−Ti complexes exhibit several notable features, including one of the largest variations in both Fe-M bond lengths (where M = B, Ti, V, Cr) and ^{57}Fe Mössbauer quadrupole splitting ($|\Delta E_Q|$) with each redox change. Additionally, the Fe K-edge XAS for the $[FeTiL]^{+/0/-}$ series reveal an unusually intense pre-edge feature, which was attributed to the substantial Fe $4p_z$ character present in the LUMO (the acceptor orbital). Hence, the combined theoretical and spectroscopic evidence shows that the d orbitals of the early transition metal (Ti) can mix with p orbitals at the late transition metal (Fe), allowing transitions to this peculiar type of LUMO to be observed. Additionally, the polarization of the core electrons on Fe can be achieved through bonding with Ti, which, to our knowledge, has not been elucidated before in any metal−metal multiply bonded system.

The collective spectroscopic and theoretical data are consistent with each redox process in the $[FeTiL]^{+/0/-}$ series being Fe-based, albeit the Ti contribution in the Fe−Ti π-bonding MOs does increase by 13% from $\mathbf{2}^{ox}$ to $\mathbf{2}^{red}$. DFT calculations reveal that the additional electron(s) populate the Fe $d_{xy}/d_{x^2-y^2}$ orbitals, which is also supported by the X-band EPR spectrum of **2**. In particular, the anisotropy of the *g*-values and ^{31}P superhyperfine coupling support the unpaired spin residing in an Fe d orbital oriented in the *xy*-plane. The filling of the Fe $d_{xy}/d_{x^2-y^2}$ orbitals is also strongly supported by the Mössbauer study. More specifically, the large variation in $|\Delta E_Q|$ upon each successive reduction stems primarily from the changes in the valence-shell contribution to the electric field gradient at Fe ($V_{ZZ}^{1c,valence}$), for which the increasingly positive values of $V_{ZZ}^{1c,valence}$ with each successive reduction directly implicate the population of the d_{xy},$d_{x^2-y^2}$ orbitals. Finally, the absence of a low-intensity pre-edge feature in the Fe K-edge XAS data of $\mathbf{2}^{red}$ is consistent with a filling of all Fe-based valence vacancies present in **2** and $\mathbf{2}^{ox}$.

Because of the limited Ti contributions in the Fe−Ti bonding MOs, we propose that the electronic structures of $\mathbf{2}^{ox}$ and **2** are well-represented by Fe^0 and Fe^{-I} and, hence Ti^{IV}. The lack of 1s → 3d transitions shows that at least spectroscopically the polarized Fe≡Ti bond in $\mathbf{2}^{red}$ gives the *appearance* of an Fe^{-II} center. However, the Ti support does play an important role in the enhanced redox flexibility of the Fe center. As negative charge accumulates on Fe, the Fe−Ti bond distance contracts. As elucidated by DFT, each Fe reduction results in better energy match between the Fe and Ti 3d orbitals, leading to increasing Ti character in the σ- and π-symmetric MOs (up to 19 and 26% in $\mathbf{2}^{red}$, respectively). The increased covalency in the Fe−Ti unit is also manifested in the Ti K-edge XAS, leading to lower energy pre-edge transitions with each reduction. This shows that even small covalent contributions in heterobimetallic complexes can have dramatic influences on the electronic and spectroscopic properties at each metal. In closing, the spectroscopic and structural changes

DOI: 10.1021/acs.inorgchem.9b00442
Inorg. Chem. 2019, 58, 6199−6214

across this redox series lend strong support to the unique redox flexibility of the Fe−Ti series, wherein subtle changes in the Fe−Ti covalency occur dynamically to accommodate the storage of electrons.

EXPERIMENTAL SECTION

General Considerations. Unless otherwise stated, all manipulations were performed under an inert atmosphere in a glovebox or using standard Schlenk techniques. Standard solvents were deoxygenated by sparging with inert gas and dried by passing through activated alumina columns of a SG Water solvent purification system. Deuterated solvents were purchased from Cambridge Isotope Laboratories, Inc. or Sigma-Aldrich. Fluorobenzene was purchased from Oakwood Chemicals. These solvents were dried over calcium hydride, degassed via freeze−pump−thaw cycles and stored over activated 4 Å molecular sieves. Elemental analyses were performed by Robertson Microlit Laboratories, Inc. (Ledgewood, NJ). All ^{1}H and ^{31}P NMR spectra were recorded on a Bruker 400 MHz spectrometer at ambient temperature unless otherwise stated. Cyclic voltammetry was performed using a CH instruments 600 electrochemical analyzer. The one-cell setup used a glassy carbon working electrode, Pt wire counter electrode, and Ag/$AgNO_3$ reference electrode in CH_3CN. Analyte solutions consisted of 0.4 M [$^{n}Bu_4N$]PF_6 and the voltammograms were referenced internally to the $FeCp_2^{0/+}$ (abbreviated as Fc^{+}/Fc) redox couple. Evans's method measurements were done in triplicate according to previously outlined procedures.[87] UV−vis−NIR spectra were collected at room temperature on a Cary-14 spectrometer. Perpendicular-mode X-band EPR spectra were recorded at 20 K with a Bruker ESP 300 spectrometer equipped with an Oxford ESR 910 liquid-helium cryostat and an Oxford temperature controller. X-band EPR spectra were simulated using the Programs esimX and MFit written by Eckhard Bill. Mössbauer data were recorded on an alternating-current constant-acceleration spectrometer. The sample temperature was maintained constant at 80 K in an Oxford Instruments Variox cryostat. The ^{57}Co/Rh source (1.8 GBq) was positioned at room temperature inside the gap of the magnet system at a zero-field position. Isomer shifts are quoted relative to Fe metal at 300 K. All metal halides were purchased either from Strem or Sigma-Aldrich and used without further purification. The protio-ligand, N(*o*-($NHCH_2P^{i}Pr_2$)C_6H_4)$_3$ (abbreviated as LH_3),[88] FeTiL (abbreviated as **2**),[30] $Ag_2B_{12}Cl_{12}$,[52] and Na[B(3,5-$(CF_3)_2$-$C_6H_3)_4$][89] ($NaBAr^{F}_4$) were synthesized according to literature procedures. TiL (abbreviated as **1**)[41] was also synthesized from literature procedures with an additional step: After isolation of crude TiL, the solid was washed with cold (−30 °C) Et_2O, then extracted using C_6H_6, yielding TiL as a bright yellow/orange powder.

Synthesis of [Ti(N(*o*-($NCH_2P^{i}Pr_2$)C_6H_4)$_3$)]BAr^{F}_4, 1^{ox}. A solution of Fc[BAr^{F}_4] (28.9 mg, 0.0276 mmol) in Et_2O (2 mL) was added dropwise to a stirred solution of **1** (20 mg, 0.0276 mmol) in Et_2O (3 mL) and stirred for 10 min. The solvent was removed in vacuo, and the solid was washed with pentane (3 × 5 mL), then placed in vacuo to yield $\mathbf{1}^{ox}$ as a green powder (40.2 mg, 92% yield). Alternatively, a solution of **2-Br** (30 mg, 0.0332 mmol) in CH_2Cl_2 (3 mL) was added to a solution of $NaBAr^{F}_4$ (29.4 mg, 0.0332 mmol) in Et_2O (4 mL), which changes to a slightly brighter shade of green. The solution is stirred for 1 h, and is then filtered through a pad of Celite. The solution is then concentrated in vacuo to yield $\mathbf{1}^{ox}$ as a green powder (52.9 mg, 97% yield). Crystals suitable for X-ray diffraction were obtained from a concentrated PhF solution of $\mathbf{1}^{ox}$ layered with hexanes. ^{1}H{^{31}P} NMR (400 MHz, THF-d_8): δ 7.79 (s, 8H, BAr^{F}_4 aryl), 7.57 (s, 4H, BAr^{F}_4 aryl), 7.23 (d, *J* = 7.7 Hz, 3H, aryl), 7.15 (app t, *J* = 7.4 Hz, 3H, aryl), 6.74 (app t, *J* = 7.7 Hz, 3H, aryl), 6.33 (d, *J* = 7.4 Hz, 3H, aryl), 4.23 (d, *J* = 13.1 Hz, 3H, CH_2), 3.79 (d, *J* = 13.1 Hz, 3H, CH_2), 2.49 (sept, *J* = 7.3 Hz, 6H, $P(CH(CH_3)_2)$, 1.49 (d, *J* = 7.3 Hz, 9H, $P(CH(CH_3)_2)$, 1.40 (d, *J* = 7.0 Hz, 9H, $P(CH(CH_3)_2)$), 1.23 (d, *J* = 7.0 Hz, 9H, $P(CH(CH_3)_2)$), 0.76 (d, *J* = 7.0 Hz, 9H, $P(CH(CH_3)_2)$). ^{31}P[^{1}H} NMR (162 MHz, THF-d_8): δ −23.8. Attempts to obtain satisfactory elemental analysis for $\mathbf{1}^{ox}$ reproducibly yielded values consistent with the addition of 1 O atom, either through reaction with water or oxygen. Anal. Calcd for $C_{71}H_{72}BN_4F_{24}P_3Ti{\cdot}O$ (%): C, 53.13; H, 4.52; N, 3.49. Found: C, 52.96; H, 4.28; N, 3.44.

Synthesis of BrFeTi(N(*o*-($NCH_2P^{i}Pr_2$)C_6H_4)$_3$), 2-Br. A solution of **1** (57.9 mg, 0.0798 mmol) in THF (4 mL) was added to $FeBr_2$ (17.2 mg, 0.0798 mmol) and stirred for 1 h, upon which the solution changes from orange/brown to dark brown. Next, a solution of **2** (62.4 mg, 0.0798 mmol) was added to the reaction solution, which immediately turns forest green. The solution is stirred overnight, after which the solution is concentrated in vacuo. The solid is then dissolved in benzene (8 mL) and filtered through a pad of Celite to yield **2-Br** as a green powder (128.0 mg, 93% yield). Single crystals suitable for X-ray diffraction were grown through diffusion of hexanes into a concentrated benzene solution of **2-Br**. ^{1}H NMR (400 MHz, C_6D_6): δ 45.9, 9.2, 7.8, 4.8, 4.0, −0.6, −9.3. Evans's method (THF-d_8): 2.97(7) μ_B. UV−vis−NIR [THF, λ_{max}, nm (ε, M^{-1} cm^{-1})]: 1268 (650), 610 (890), 320(sh) (15 900), 292(sh) (18 600). Anal. Calcd for $C_{39}H_{60}N_4P_3TiFeBr{\cdot}0.5(C_6H_6)$ (%): C, 56.02; H, 7.05; N, 6.22. Found: C, 56.13; H, 7.01; N, 5.95.

Synthesis of [FeTi(N(*o*-($NCH_2P^{i}Pr_2$)C_6H_4)$_3$)]BAr^{F}_4, [2^{ox}]BAr^{F}_4. A solution of **2-Br** (82.2 mg, 0.0909 mmol) in fluorobenzene (4 mL) was added to a solution of $NaBAr^{F}_4$ (84.2 mg, 0.0999 mmol) in fluorobenzene (2 mL), which immediately changes from forest green to dark red/brown. The solution is stirred for 2 h, and is then filtered through a pad of Celite. After removing the solvent in vacuo, the brown solid was extracted using toluene cooled to −78 °C (5 mL) and filtered through another pad of Celite. The filtrate was then concentrated in vacuo to yield $\mathbf{2}^{ox}$ as a brown powder (128.2 mg, 90% yield). ^{1}H NMR (400 MHz, C_6D_6): δ 58.3, 29.5, 12.4, 9.5, 7.8, 7.6, −7.0, −9.6. Evans's method (THF-d_8): 2.99(8) μ_B. UV−vis−NIR [THF, λ_{max}, nm (ε, M^{-1} cm^{-1})]: 1279 (370), 1100 (310), 416 (3750), 304 (22 900). Attempts to obtain satisfactory elemental analysis for [$\mathbf{2}^{ox}$]BAr^{F}_4 reproducibly yielded values consistent with the addition of 3 O atoms, either through reaction of $\mathbf{2}^{ox}$ with water or oxygen. Anal. Calcd for $C_{71}H_{72}BN_4F_{24}P_3TiFe{\cdot}3O$ (%): C, 50.38; H, 4.29; N, 3.31. Found: C, 50.42; H, 4.51; N, 3.30.

Synthesis of $K(THF)_3$[FeTi(N(*o*-($NCH_2P^{i}Pr_2$)C_6H_4)$_3$)], 2^{red}. A solution of FeTiL (100.3 mg, 0.1283 mmol) in THF (8 mL) was added to a slurry of KC_8 (36.4 mg, 0.2695 mmol) and allowed to stir for 1 h. The yellow/brown solution quickly became dark red. The solvent was removed in vacuo. The solid is then washed with benzene (3 × 4 mL) or until the washings were clear. Then, the solid was dissolved in a 3:1 mixture of hexanes/THF (3 × 5 mL), then filtered through a pad of Celite until the filtrate was clear. The solution was concentrated in vacuo until microcrystalline solids began to appear on the walls, upon which the solution was cooled to −25 °C overnight, yielding dark brown crystals (128.1 mg, 45% yield). Single crystals suitable for X-ray diffraction were isolated using this method. ^{1}H{^{31}P} NMR (400 MHz, THF-d_8): δ 6.61 (app t, *J* = 7.3 Hz, 3H, aryl), 6.38 (d, *J* = 7.2 Hz, 3H, aryl), 6.07 (d, *J* = 7.3 Hz, 3H, aryl), 5.68 (app t, *J* = 7.2 Hz, 3H, aryl), 5.28 (br, 2H, CH_2), 4.92 (br, 2H, CH_2), 3.61 (AA′BB′, THF CH_2), 2.87 (br, 4H, $P(CH(CH_3)_2)$, 1.77 (AA′BB′, THF CH_2) 1.69 (br, 9H, $P(CH(CH_3)_2)$, 1.48 (br, 9H, $P(CH(CH_3)_2)$, 1.08 (br, 9H, $P(CH(CH_3)_2)$, 0.35 (br, 9H, $P(CH(CH_3)$). ^{31}P[^{1}H} NMR (162 MHz, THF-d_8, −83 °C): δ 41.3 (s). UV−vis−NIR [THF, λ_{max}, nm (ε, M^{-1} cm^{-1})]: 690(sh) (650), 447(sh) (6430), 375(sh) (9400), 318 (37 600). Elemental analysis of $\mathbf{2}^{red}$ consistently yielded values that were too low in C and H. The closest result to theory is shown. Anal. Calcd for [$C_{39}H_{60}N_4P_3TiFeK$] (%): C, 57.08; H, 7.37; N, 6.83. Found: C, 54.49; H, 7.29; N, 6.11.

X-ray Crystallography and Structure Refinement Details. Single crystals of **1** suitable for X-ray diffraction were grown by cooling a concentrated solution of **1** in diethyl ether to −25 °C. Single crystals of [$\mathbf{2}^{ox}$]$_2$[$B_{12}Cl_{12}$] were grown by layering **2** over a solution of 0.5 equiv of $Ag_2B_{12}Cl_{12}$ in THF. A plate of **1** (0.27 × 0.20 × 0.10 mm), a plate of [$\mathbf{1}^{ox}$]BAr^{F}_4 (0.13 × 0.12 × 0.05 mm), a block of [$K(THF)_3$]$\mathbf{2}^{red}$ (0.08 × 0.06 × 0.03 mm), a block of **2-Br** (0.17 × 0.15 × 0.15 mm), and a block of [$\mathbf{2}^{ox}$]$_2$[$B_{12}Cl_{12}$] (0.05 × 0.04 × 0.04 mm) were mounted on a 100 μm MiTeGen microloop and placed on a Bruker PHOTON-II CMOS diffractometer for data collection at

DOI: 10.1021/acs.inorgchem.9b00442
Inorg. Chem. 2019, 58, 6199−6214

Table 6. Crystallographic Details for 1, 1^{ox}, $[K(THF)_3]2^{red}$, 2-Br, and $[2^{ox}]_2[B_{12}Cl_{12}]$

	1	$[1^{ox}]BAr^F{}_4$	$[K(THF)_3]2^{red}$	$[2^{ox}]_2[B_{12}Cl_{12}]$	2-Br
chemical formula	$C_{39}H_{60}N_4P_3Ti$	$C_{39}H_{60}N_4P_3Ti{\cdot}C_{32}H_{12}F_{24}B{\cdot}1.5(C_6H_{14})$	$C_{51}H_{84}N_4P_3TiFeO_3K\ C_4H_8O$	$C_{39}H_{60}N_4P_3TiFe{\cdot}0.5(B_{12}Cl_{12}){\cdot}0.5(C_4H_8O)$	$C_{39}H_{60}N_4P_3TiFeBr{\cdot}C_6H_{14}$
fw	725.72	1718.20	1109.08	2154.33	947.65
cryst syst	monoclinic	triclinic	monoclinic	trigonal	monoclinic
space group	$P2_1/n$	$P\bar{1}$	Pn	$P\bar{3}c1$	$P2_1/c$
a (Å)	11.4570(2)	14.3310(4)	12.4492(7)	14.9687(4)	11.8596(8)
b (Å)	19.5908(4)	14.5231(4)	14.8815(8)	14.9687(4)	16.2862(12)
c (Å)	17.4139(3)	21.7918(6)	16.5942(8)	26.3435(7)	24.3211(17)
α (deg)	90	73.4696(9)	90	90	90
β (deg)	93.3095(8)	73.2797(9)	110.751(2)	90	100.234(2)
γ (deg)	90	77.4976(9)	90	120	90
V (Å^3)	3902.06(12)	4119.2(2)	2874.9(3)	5111.8(3)	4622.8(6)
Z	4	2	2	4	4
D_{calcd} (g cm^{-3})	1.235	1.281	1.281	1.376	1.362
λ (Å), μ (mm^{-1})	1.54178, 3.257	0.71073, 0.262	0.71073, 0.593	0.71073, 0.880	0.71073, 1.490
T (K)	123(2)	123(2)	123(2)	123(2)	123(2)
θ range (deg)	3.399−74.55	2.198−27.485	2.243−30.543	2.204−29.572	2.192−30.530
reflns collected	45070	74880	78701	121213	97962
unique reflns	6977	12615	15303	3482	10845
data/restraints/param	7983/0/436	18899/3/989	17550/2/648	4790/0/185	14112/3/533
R_1, wR_2 ($I > 2\sigma(I)$)	0.0337, 0.0836	0.0648, 0.1652	0.0385, 0.0881	0.0457, 0.1015	0.0347, 0.0772
R_1, wR_2 (all data)	0.0406, 0.0874	0.1014, 0.1847	0.0500, 0.0933	0.0743, 0.1122	0.0581, 0.0907

DOI: 10.1021/acs.inorgchem.9b00442
Inorg. Chem. 2019, 58, 6199−6214

123(2) K. The data collection was carried out using Cu Kα (for **1**) or Mo Kα radiation (for all others) with normal parabolic mirrors. The data intensities were corrected for absorption and decay with SADABS.[90] Final cell constants were obtained from least-squares fits from all reflections. Crystal structure solution was done through intrinsic phasing (SHELXT-2014/5),[91] which provided most non-hydrogen atoms. Full matrix least-squares/difference Fourier cycles were performed (using SHELXL-2016/6 and GUI ShelXle)[92,93] to locate the remaining non-hydrogen atoms. All non-hydrogen atoms were refined with anisotropic displacement parameters. Hydrogen atoms were placed in ideal positions and refined as riding atoms with relative isotropic displacement parameters. The crystal structures of $[\mathbf{1}^{ox}]BAr^{F}_{4}$ contained two hexane molecules that were disordered over both a crystallographic inversion center and a general position. All attempts to model this solvent were unsuccessful. Additionally, $[\mathbf{2}^{ox}]_2[B_{12}Cl_{12}]$ crystallized in the space group $P\bar{3}c1$ and contained an unidentified solvent molecule near the $\bar{3}$ rotoinversion axes. Thus, the SQUEEZE function of the PLATON program was used to remove these solvent molecules from the void space.[94] The SQUEEZE function removed 144 electrons from a void-space volume of 645 Å^3 in $[\mathbf{1}^{ox}]BAr^{F}_{4}$ and 80 electrons from a void-space volume of 411 Å^3 in $[\mathbf{2}^{ox}]_2[B_{12}Cl_{12}]$. These values are consistent with the presence of approximately 3 hexane and 2 THF molecules in the unit cells of $[\mathbf{1}^{ox}]BAr^{F}_{4}$ and $[\mathbf{2}^{ox}]_2[B_{12}Cl_{12}]$, respectively. Crystallographic data are summarized in Table 6.

X-ray Absorption Spectroscopy (XAS). *Sample Preparation, Measurements and Data Analysis.* Solid samples for X-ray spectroscopic analysis were prepared in an inert-atmosphere glovebox. For Fe and Ti K-edge XAS measurements, the solid samples were finely ground using an agate mortar and pestle with boron nitride (BN) into a homogeneous mixture comprising 5% w/w photo-absorbing metal. These mixtures were pressed into 1 mm Al spacers and sealed with 38 μm Kapton tape. Fe and Ti K-edge XAS spectra were obtained at the Stanford Synchrotron Radiation Lightsource (SSRL) at beamline 9−3 under ring conditions of 3 GeV and 500 mA. A Si(220) double-crystal monochromator was used for energy selection. For Fe, a Rh-coated mirror (set to an energy cutoff of 9 keV) was used for harmonic rejection. Incident energy calibrations were performed by assigning the first inflection points of Fe and Ti foil spectra to 7111.2 and 4966 eV, respectively. Data were collected in fluorescence mode using a Canberra 100-element Ge array detector. Samples were maintained at 10 K in an Oxford liquid He flow cryostat. For spectra measured by fluorescence detection, elastic scatter into the detector was attenuated using a Soller slit with upstream Co or Sc filters. Data were collected from 6784 to 7510 eV for Fe and 4734 to 5360 eV for Ti. Multiple scans were measured and averaged with SIXPACK[95] software package. No spectral changes due to photodamage were observed after multiple scans for these complexes. Data were normalized to postedge jumps of 1.0 (Ti: 4985 eV, Fe: 7130 eV) in SIXPACK by applying a Gaussian normalization for the pre-edge and a quadratic normalization for the postedge to produce the final spectra. The final processed spectra were plotted using Igor Pro 6.37.

Computational Details. Density functional theory (DFT) calculations were conducted to understand the electronic structures of $\mathbf{2}^{ox}$, **2** and $\mathbf{2}^{red}$, and to calculate their Mössbauer parameters and Fe/Ti K-edge XAS spectra. Different DFT methods were employed for the Mössbauer and XAS calculations, as detailed below. Specifically, the electronic structures shown in Figure 4 and Table 2 (also Figure S19 and Table S4) were obtained from the Mössbauer study, whereas the electronic structures derived from the XAS study are shown in Figure S20 and Table S5. Notably, the different DFT methods all yielded highly similar electronic structures.

Mössbauer Spectroscopy. DFT calculations on Mössbauer parameters were performed using the ORCA 4.0 package.[96] Starting from the crystal structure coordinates, all hydrogen atoms were optimized while the positions of all the other atoms were constrained, using the functional BP86 and the basis set def2-SVP for all atoms. For estimation of the Mössbauer parameters, single-point calculations were then carried out on the resulting geometries at the B3LYP level of theory, where the basis set CP(PPP)[97] having an uncontracted core-region was used for iron, and the basis set def2-TZVP[98] was used for all other atoms. Notably, the use of the B3LYP functional and CP(PPP) basis set have previously been shown to satisfactorily reproduce Mössbauer parameters.[99−101] All calculations were carried out in gas phase. The RIJCOSX algorithm was used to speed up the Hartree−Fock exchange. The quasi-restricted orbitals (QROs)[102] generated by the above single-point calculations were localized using Pipek-Mezey algorithm[103] for the Löwdin population analysis and quadrupole splitting contribution breakdown.

The isomer shift (δ) was computed from the electron density at the iron nucleus (ρ_0) by using the following equation,

$$\delta = \alpha(\rho_0 - C) + \beta$$

Parameters α, β, and C were determined by a linear progression for a series of iron complexes with different oxidation states and spin multiplicities. Specifically, one first computes the electron density at the iron nucleus for each complex and then sets up a linear correlation between the isomer shift measured experimentally and the calculated density.[74] Consequently, the linear equation obtained can only be used to predict the isomer shifts of iron complexes that feature similar bonding to the preselected complexes. In the present case, the calculated isomer shifts using the parameters reported[99] were systematically underestimated. No bimetallic iron complexes that involve metal−metal bonding are included in this training set. The same situation was found for isomer shift calculations on seven related bimetallic complexes. On the basis of these observations, we decided to design a new calibration curve from the calculated density and experimental isomer shifts of these seven complexes, which was used for isomer shift calculations in the present study. The new set of the parameters were $\alpha = -0.316$, $\beta = 2.661$, and $C = 11810$. The details are shown in Table S8 and Figure S26.

XAS. DFT calculations were performed to directly correlate X-ray spectroscopy to electronic structure. All electronic structure and spectroscopic calculations were performed using the ORCA 3.03 package.[104,105] Starting from crystal structure coordinates, the structures were fully geometry-optimized using the BP86[106,107] functional, the zeroth-order regular approximation for relativistic effects (ZORA) as implemented by van Wüllen[108−110] and scalar relativistically recontracted Ahlrich's def2-TZVP(-f)(def2-TZVP(-f)-ZORA)[98,111,112] basis set, followed by frequency calculations to ensure that no imaginary vibrational modes were present. Solvation was modeled with the conductor like screening model (COSMO) using an infinite dielectric.[113] Fe and Ti K-edge XAS spectra were calculated using TD-DFT calculations with both geometry optimized and crystallographic coordinates utilizing B3LYP functional,[114] the CP(PPP)[74,97] basis set on the transition metals (Ti and Fe) using an integration grid accuracy of 7, and the def2-TZVP(-f)-ZORA basis set on all other atoms. Calculations with hybrid functionals used the RIJCOSX algorithm to speed the calculation of Hartree−Fock exchange.[115] Error in core potential energetics were evaluated by plotting the calculated XAS peak energies against experimental peak energies (Figure S30). The use of B3LYP and the CP(PPP) basis set have previously been shown to satisfactorily reproduce Fe K-edge XAS data.[116,117]

■ ASSOCIATED CONTENT

Supporting Information

The Supporting Information is available free of charge on the ACS Publications website at DOI: 10.1021/acs.inorgchem.9b00442.

Cyclic voltammetry data, NMR results, X-ray crystallography data, EPR spectra and discussion, UV−vis−NIR spectra and absorbance data, molecular orbital analysis, Mössbauer parameters and isomer shifts, X-ray absorption spectra (PDF)

Cartesian coordinate data for complexes **1**, $\mathbf{1}^{ox}$, **2**, **2-Br**, $\mathbf{2}^{ox}$, and $\mathbf{2}^{red}$ (ZIP)

DOI: 10.1021/acs.inorgchem.9b00442
Inorg. Chem. 2019, 58, 6199−6214

Accession Codes

CCDC 1863841−1863845 contain the supplementary crystallographic data for this paper. These data can be obtained free of charge via www.ccdc.cam.ac.uk/data_request/cif, or by emailing data_request@ccdc.cam.ac.uk, or by contacting The Cambridge Crystallographic Data Centre, 12 Union Road, Cambridge CB2 1EZ, UK; fax: +44 1223 336033.

AUTHOR INFORMATION

Corresponding Authors

*E-mail: shengfa.ye@kofo.mpg.de (S.Y.).
*E-mail: kml236@cornell.edu (K.M.L.).
*E-mail: clu@umn.edu (C.C.L.).

ORCID

Stephen Sproules: 0000-0003-3587-0375
Eckhard Bill: 0000-0001-9138-3964
Varinia Bernales: 0000-0002-8446-7956
Laura Gagliardi: 0000-0001-5227-1396
Shengfa Ye: 0000-0001-9747-1412
Kyle M. Lancaster: 0000-0001-7296-128X
Connie C. Lu: 0000-0002-5162-9250

Author Contributions

#These authors contributed equally.

Notes

The authors declare no competing financial interest.

ACKNOWLEDGMENTS

We thank Prof. John Lipscomb for access to the EPR spectrometer, Dr. Ryan Cammarota for collecting EPR data, Bernd Mienert for collecting the Mössbauer spectra, and Dr. Victor G. Young, Jr. for assistance with X-ray crystallography. C.C.L. acknowledges the NSF (CHE-1800110) for support of the synthetic work. K.M.L acknowledges NSF (CHE-1454455) and the Alfred P. Sloan Foundation for support. M.T., E.B., and S.Y. also gratefully acknowledge the financial support from the Max-Planck Society, in particular the joint work space between MPI-CEC and MPI-KOFO. X-ray diffraction experiments were performed using a crystal diffractometer purchased through a grant from NSF/MRI (1229400) and the University of Minnesota. The work at MPI has received funding from the European Union's Horizon 2020 research and innovation programme under Grant Agreement No. 675020 (675020-MSCA-ITN-2015-ETN). Use of the Stanford Synchrotron Radiation Lightsource, SLAC National Accelerator Laboratory, is supported by the U.S. Department of Energy, Office of Science, Office of Basic Energy Sciences under Contract No. DE-AC02-76SF00515. The SSRL Structural Molecular Biology Program is supported by the DOE Office of Biological and Environmental Research, and by the National Institutes of Health, National Institute of General Medical Sciences (including P41GM103393) . The contents of this publication are solely the responsibility of the authors and do not necessarily represent the official views of NIGMS or NIH.

DEDICATION

We dedicate this paper to our mentor and friend, Dr. Karl Wieghardt, on the occasion of his 77th birthday.

REFERENCES

(1) Sono, M.; Roach, M. P.; Coulter, E. D.; Dawson, J. H. Heme-Containing Oxygenases. *Chem. Rev.* **1996**, *96*, 2841.
(2) Kovaleva, E. G.; Lipscomb, J. D. Versatility of biological non-heme Fe(II) centers in oxygen activation reactions. *Nat. Chem. Biol.* **2008**, *4*, 186.
(3) Jasniewski, A. J.; Que, L. Dioxygen Activation by Nonheme Diiron Enzymes: Diverse Dioxygen Adducts, High-Valent Intermediates, and Related Model Complexes. *Chem. Rev.* **2018**, *118*, 2554.
(4) Kal, S.; Que, L. Dioxygen activation by nonheme iron enzymes with the 2-His-1-carboxylate facial triad that generate high-valent oxoiron oxidants. *JBIC, J. Biol. Inorg. Chem.* **2017**, *22*, 339.
(5) Einsle, O.; Tezcan, F. A.; Andrade, S. L. A.; Schmid, B.; Yoshida, M.; Howard, J. B.; Rees, D. C. Nitrogenase MoFe-Protein at 1.16 Å Resolution: A Central Ligand in the FeMo-Cofactor. *Science* **2002**, *297*, 1696.
(6) Cassani, C.; Bergonzini, G.; Wallentin, C.-J. Active Species and Mechanistic Pathways in Iron-Catalyzed C−C Bond-Forming Cross-Coupling Reactions. *ACS Catal.* **2016**, *6*, 1640.
(7) Collman, J. P. Disodium tetracarbonylferrate, a transition metal analog of a Grignard reagent. *Acc. Chem. Res.* **1975**, *8*, 342.
(8) Daifuku, S. L.; Al-Afyouni, M. H.; Snyder, B. E. R.; Kneebone, J. L.; Neidig, M. L. A Combined Mössbauer, Magnetic Circular Dichroism, and Density Functional Theory Approach for Iron Cross-Coupling Catalysis: Electronic Structure, In Situ Formation, and Reactivity of Iron-Mesityl-Bisphosphines. *J. Am. Chem. Soc.* **2014**, *136*, 9132.
(9) Zell, T.; Milstein, D. Hydrogenation and Dehydrogenation Iron Pincer Catalysts Capable of Metal−Ligand Cooperation by Aromatization/Dearomatization. *Acc. Chem. Res.* **2015**, *48*, 1979.
(10) Bauer, I.; Knölker, H.-J. Iron Catalysis in Organic Synthesis. *Chem. Rev.* **2015**, *115*, 3170.
(11) Nam, W. Synthetic Mononuclear Nonheme Iron−Oxygen Intermediates. *Acc. Chem. Res.* **2015**, *48*, 2415.
(12) McDonald, A. R.; Que, L. High-valent nonheme iron-oxo complexes: Synthesis, structure, and spectroscopy. *Coord. Chem. Rev.* **2013**, *257*, 414.
(13) Bedford, R. B. How Low Does Iron Go? Chasing the Active Species in Fe-Catalyzed Cross-Coupling Reactions. *Acc. Chem. Res.* **2015**, *48*, 1485.
(14) Martin, R.; Fürstner, A. Cross-Coupling of Alkyl Halides with Aryl Grignard Reagents Catalyzed by a Low-Valent Iron Complex. *Angew. Chem., Int. Ed.* **2004**, *43*, 3955.
(15) Chin, H. B.; Bau, R. The crystal structure of disodium tetracarbonylferrate. Distortion of the tetracarbonylferrate(2-) anion in the solid state. *J. Am. Chem. Soc.* **1976**, *98*, 2434.
(16) Brennessel, W. W.; Ellis, J. E. [Fe(CNXyl)4]2−: An Isolable and Structurally Characterized Homoleptic Isocyanidemetalate Dianion. *Angew. Chem., Int. Ed.* **2007**, *46*, 598.
(17) Mokhtarzadeh, C. C.; Moore, C. E.; Rheingold, A. L.; Figueroa, J. S. Terminal Iron Carbyne Complexes Derived from Arrested CO2 Reductive Disproportionation. *Angew. Chem., Int. Ed.* **2017**, *56*, 10894.
(18) Mokhtarzadeh, C. C.; Margulieux, G. W.; Carpenter, A. E.; Weidemann, N.; Moore, C. E.; Rheingold, A. L.; Figueroa, J. S. Synthesis and Protonation of an Encumbered Iron Tetraisocyanide Dianion. *Inorg. Chem.* **2015**, *54*, 5579.
(19) Jonas, K.; Schieferstein, L.; Krüger, C.; Tsay, Y.-H. Tetrakis-(ethylene)irondilithium and Bis(η4−1,5-cy-clooctadiene)-irondilithium. *Angew. Chem., Int. Ed. Engl.* **1979**, *18*, 550.
(20) Kruck, T.; Prasch, A. Synthese und Struktur der Tetrakis-(trifluorphosphin)-metalldihydride und -metallate(-II) von Eisen, Ruthenium und Osmium. *Z. Anorg. Allg. Chem.* **1969**, *371*, 1.
(21) Schnöckelborg, E.-M.; Khusniyarov, M. M.; de Bruin, B.; Hartl, F.; Langer, T.; Eul, M.; Schulz, S.; Pöttgen, R.; Wolf, R. Unraveling the Electronic Structures of Low-Valent Naphthalene and Anthracene Iron Complexes: X-ray, Spectroscopic, and Density Functional Theory Studies. *Inorg. Chem.* **2012**, *51*, 6719.
(22) Wolczanski, P. T. Flipping the Oxidation State Formalism: Charge Distribution in Organometallic Complexes As Reported by Carbon Monoxide. *Organometallics* **2017**, *36*, 622.

DOI: 10.1021/acs.inorgchem.9b00442
Inorg. Chem. 2019, 58, 6199−6214

(23) Thompson, N. B.; Green, M. T.; Peters, J. C. Nitrogen Fixation via a Terminal Fe(IV) Nitride. *J. Am. Chem. Soc.* **2017**, *139*, 15312.
(24) Enemark, J. H.; Feltham, R. D. Principles of structure, bonding, and reactivity for metal nitrosyl complexes. *Coord. Chem. Rev.* **1974**, *13*, 339.
(25) Parkin, G. A Simple Description of the Bonding in Transition-Metal Borane Complexes. *Organometallics* **2006**, *25*, 4744.
(26) Hill, A. F. An Unambiguous Electron-Counting Notation for Metallaboratranes. *Organometallics* **2006**, *25*, 4741.
(27) Wu, B.; Wilding, M. J. T.; Kuppuswamy, S.; Bezpalko, M. W.; Foxman, B. M.; Thomas, C. M. Exploring Trends in Metal−Metal Bonding, Spectroscopic Properties, and Conformational Flexibility in a Series of Heterobimetallic Ti/M and V/M Complexes (M = Fe, Co, Ni, and Cu). *Inorg. Chem.* **2016**, *55*, 12137.
(28) Moret, M.-E.; Peters, J. C. Terminal Iron Dinitrogen and Iron Imide Complexes Supported by a Tris(phosphino)borane Ligand. *Angew. Chem., Int. Ed.* **2011**, *50*, 2063.
(29) Eisenhart, R. J.; Rudd, P. A.; Planas, N.; Boyce, D. W.; Carlson, R. K.; Tolman, W. B.; Bill, E.; Gagliardi, L.; Lu, C. C. Pushing the Limits of Delta Bonding in Metal−Chromium Complexes with Redox Changes and Metal Swapping. *Inorg. Chem.* **2015**, *54*, 7579.
(30) Eisenhart, R. J.; Clouston, L. J.; Lu, C. C. Configuring Bonds between First-Row Transition Metals. *Acc. Chem. Res.* **2015**, *48*, 2885.
(31) Clouston, L. J.; Bernales, V.; Cammarota, R. C.; Carlson, R. K.; Bill, E.; Gagliardi, L.; Lu, C. C. Heterobimetallic Complexes That Bond Vanadium to Iron, Cobalt, and Nickel. *Inorg. Chem.* **2015**, *54*, 11669.
(32) Clouston, L. J.; Siedschlag, R. B.; Rudd, P. A.; Planas, N.; Hu, S.; Miller, A. D.; Gagliardi, L.; Lu, C. C. Systematic Variation of Metal−Metal Bond Order in Metal−Chromium Complexes. *J. Am. Chem. Soc.* **2013**, *135*, 13142.
(33) Kuppuswamy, S.; Bezpalko, M. W.; Powers, T. M.; Wilding, M. J. T.; Brozek, C. K.; Foxman, B. M.; Thomas, C. M. A series of C3-symmetric heterobimetallic Cr-M (M = Fe, Co and Cu) complexes. *Chem. Sci.* **2014**, *5*, 1617.
(34) Krogman, J. P.; Thomas, C. M. Metal-metal multiple bonding in C3-symmetric bimetallic complexes of the first row transition metals. *Chem. Commun.* **2014**, *50*, 5115.
(35) Krogman, J. P.; Gallagher, J. R.; Zhang, G.; Hock, A. S.; Miller, J. T.; Thomas, C. M. Assignment of the oxidation states of Zr and Co in a highly reactive heterobimetallic Zr/Co complex using X-ray absorption spectroscopy (XANES). *Dalton Trans* **2014**, *43*, 13852.
(36) Dunn, P. L.; Carlson, R. K.; Tonks, I. A. Synthesis and characterization of triply-bonded titanium-iron complexes supported by 2-(diphenylphosphino)pyrrolide ligands. *Inorg. Chim. Acta* **2017**, *460*, 43.
(37) Allen, L. C. Electronegativity is the average one-electron energy of the valence-shell electrons in ground-state free atoms. *J. Am. Chem. Soc.* **1989**, *111*, 9003.
(38) Mann, J. B.; Meek, T. L.; Allen, L. C. Configuration Energies of the Main Group Elements. *J. Am. Chem. Soc.* **2000**, *122*, 2780.
(39) Mann, J. B.; Meek, T. L.; Knight, E. T.; Capitani, J. F.; Allen, L. C. Configuration Energies of the d-Block Elements. *J. Am. Chem. Soc.* **2000**, *122*, 5132.
(40) Karen, P. Oxidation State, A Long-Standing Issue! *Angew. Chem., Int. Ed.* **2015**, *54*, 4716.
(41) Clouston, L. J.; Bernales, V.; Carlson, R. K.; Gagliardi, L.; Lu, C. C. Bimetallic Cobalt−Dinitrogen Complexes: Impact of the Supporting Metal on N2 Activation. *Inorg. Chem.* **2015**, *54*, 9263.
(42) Herrmann, W. A.; Denk, M.; Albach, R. W.; Behm, J.; Herdtweck, E. Cyclische Metall(IV)-amide. *Chem. Ber.* **1991**, *124*, 683.
(43) Pavlishchuk, V. V.; Addison, A. W. Conversion constants for redox potentials measured versus different reference electrodes in acetonitrile solutions at 25°C. *Inorg. Chim. Acta* **2000**, *298*, 97.
(44) Friis, E. P.; Andersen, J. E. T.; Madsen, L. L.; Bonander, N.; Møller, P.; Ulstrup, J. Dynamics of Pseudomonas aeruginosa azurin and its Cys3Ser mutant at single-crystal gold surfaces investigated by cyclic voltammetry and atomic force microscopy. *Electrochim. Acta* **1998**, *43*, 1114.
(45) Clouston, L. J. Understanding Metal-Metal Bonds in Heterobimetallic Complexes and Their Use as Catalysts for Dinitrogen Conversion. Ph.D. Thesis. University of Minnesota, 2016.
(46) Cammarota, R. C.; Clouston, L. J.; Lu, C. C. Leveraging molecular metal−support interactions for H2 and N2 activation. *Coord. Chem. Rev.* **2017**, *334*, 100.
(47) Greenwood, B. P.; Forman, S. I.; Rowe, G. T.; Chen, C.-H.; Foxman, B. M.; Thomas, C. M. Multielectron Redox Activity Facilitated by Metal−Metal Interactions in Early/Late Heterobimetallics: Co/Zr Complexes Supported by Phosphinoamide Ligands. *Inorg. Chem.* **2009**, *48*, 6251.
(48) Kuppuswamy, S.; Powers, T. M.; Krogman, J. P.; Bezpalko, M. W.; Foxman, B. M.; Thomas, C. M. Vanadium-iron complexes featuring metal-metal multiple bonds. *Chem. Sci.* **2013**, *4*, 3557.
(49) Harman, W. H.; Peters, J. C. Reversible H2 Addition across a Nickel−Borane Unit as a Promising Strategy for Catalysis. *J. Am. Chem. Soc.* **2012**, *134*, 5080.
(50) Suess, D. L. M.; Tsay, C.; Peters, J. C. Dihydrogen Binding to Isostructural S = 1/2 and S = 0 Cobalt Complexes. *J. Am. Chem. Soc.* **2012**, *134*, 14158.
(51) Whited, M. T.; Zhang, J.; Ma, S.; Nguyen, B. D.; Janzen, D. E. Silylene-assisted hydride transfer to CO2 and CS2 at a [P2Si]Ru pincer-type complex. *Dalton Trans* **2017**, *46*, 14757.
(52) Gu, W.; Ozerov, O. V. Exhaustive Chlorination of [B12H12]2− without Chlorine Gas and the Use of [B12Cl12]2− as a Supporting Anion in Catalytic Hydrodefluorination of Aliphatic C−F Bonds. *Inorg. Chem.* **2011**, *50*, 2726.
(53) Pauling, L. Atomic Radii and Interatomic Distances in Metals. *J. Am. Chem. Soc.* **1947**, *69*, 542.
(54) Cotton, F. A., Murillo, C. A., Walton, R. A., Eds. *Multiple Bonds Between Metal Atoms*, 3rd ed.; Springer Science and Business Media, Inc.: New York, 2005; p 44.
(55) Noor, A.; Wagner, F. R.; Kempe, R. Metal−Metal Distances at the Limit: A Coordination Compound with an Ultrashort Chromium−Chromium Bond. *Angew. Chem., Int. Ed.* **2008**, *47*, 7246.
(56) Noor, A.; Glatz, G.; Müller, R.; Kaupp, M.; Demeshko, S.; Kempe, R. Metal−Metal Distances at the Limit: Cr−Cr 1.73 Å − the Importance of the Ligand and its Fine Tuning. *Z. Anorg. Allg. Chem.* **2009**, *635*, 1149.
(57) Noor, A.; Bauer, T.; Todorova, T. K.; Weber, B.; Gagliardi, L.; Kempe, R. The Ligand-Based Quintuple Bond-Shortening Concept and Some of Its Limitations. *Chem. - Eur. J.* **2013**, *19*, 9825.
(58) Hsu, H.; Yu, J.-S. K.; Yen, C.-H.; Lee, G.-H.; Wang, T.; Tsai, Y.-C. Quintuply-Bonded Dichromium(I) Complexes Featuring Metal−Metal Bond Lengths of 1.74 Å. *Angew. Chem., Int. Ed.* **2008**, *47*, 9933.
(59) Kreisel, K. A.; Yap, G. P. A.; Dmitrenko, O.; Landis, C. R.; Theopold, K. H. The Shortest Metal−Metal Bond Yet: Molecular and Electronic Structure of a Dinuclear Chromium Diazadiene Complex. *J. Am. Chem. Soc.* **2007**, *129*, 14162.
(60) Nguyen, T.; Sutton, A. D.; Brynda, M.; Fettinger, J. C.; Long, G. J.; Power, P. P. Synthesis of a Stable Compound with Fivefold Bonding Between Two Chromium(I) Centers. *Science* **2005**, *310*, 844.
(61) Wolf, R.; Ni, C.; Nguyen, T.; Brynda, M.; Long, G. J.; Sutton, A. D.; Fischer, R. C.; Fettinger, J. C.; Hellman, M.; Pu, L.; Power, P. P. Substituent Effects in Formally Quintuple-Bonded ArCrCrAr Compounds (Ar = Terphenyl) and Related Species. *Inorg. Chem.* **2007**, *46*, 11277.
(62) Wu, L.-C.; Hsu, C.-W.; Chuang, Y.-C.; Lee, G.-H.; Tsai, Y.-C.; Wang, Y. Bond Characterization on a Cr−Cr Quintuple Bond: A Combined Experimental and Theoretical Study. *J. Phys. Chem. A* **2011**, *115*, 12602.
(63) Huang, Y.-L.; Lu, D.-Y.; Yu, H.-C.; Yu, J.-S. K.; Hsu, C.-W.; Kuo, T.-S.; Lee, G.-H.; Wang, Y.; Tsai, Y.-C. Stepwise Construction of the CrCr Quintuple Bond and Its Destruction upon Axial Coordination. *Angew. Chem., Int. Ed.* **2012**, *51*, 7781.

DOI: 10.1021/acs.inorgchem.9b00442
Inorg. Chem. 2019, 58, 6199−6214

(64) Rudd, P. A.; Liu, S.; Planas, N.; Bill, E.; Gagliardi, L.; Lu, C. C. Multiple Metal−Metal Bonds in Iron−Chromium Complexes. *Angew. Chem., Int. Ed.* **2013**, *52*, 4449.
(65) Greer, S. M.; McKay, J.; Gramigna, K. M.; Thomas, C. M.; Stoian, S. A.; Hill, S. Probing Fe−V Bonding in a C3-Symmetric Heterobimetallic Complex. *Inorg. Chem.* **2018**, *57*, 5870.
(66) Rudd, P. A.; Planas, N.; Bill, E.; Gagliardi, L.; Lu, C. C. Dinitrogen Activation at Iron and Cobalt Metallalumatranes. *Eur. J. Inorg. Chem.* **2013**, *2013*, 3898.
(67) Vollmer, M. V.; Xie, J.; Cammarota, R. C.; Young, V. G., Jr.; Bill, E.; Gagliardi, L.; Lu, C. C. Formal Nickelate(−I) Complexes Supported by Group 13 Ions. *Angew. Chem., Int. Ed.* **2018**, *57*, 7815.
(68) Watanabe, T.; Fujiwara, S. EPR studies of Ti(III) chelates in aqueous solution; The nature of chemical bonding and EPR relaxation mechanism. *J. Magn. Reson.* **1970**, *2*, 103.
(69) Maurelli, S.; Livraghi, S.; Chiesa, M.; Giamello, E.; Van Doorslaer, S.; Di Valentin, C.; Pacchioni, G. Hydration Structure of the Ti(III) Cation as Revealed by Pulse EPR and DFT Studies: New Insights into a Textbook Case. *Inorg. Chem.* **2011**, *50*, 2385.
(70) Morra, E.; Maurelli, S.; Chiesa, M.; Van Doorslaer, S. Probing the coordination environment of Ti3+ ions coordinated to nitrogen-containing Lewis bases. *Phys. Chem. Chem. Phys.* **2015**, *17*, 20853.
(71) Cammarota, R. C.; Vollmer, M. V.; Xie, J.; Ye, J.; Linehan, J. C.; Burgess, S. A.; Appel, A. M.; Gagliardi, L.; Lu, C. C. A Bimetallic Nickel−Gallium Complex Catalyzes CO2 Hydrogenation via the Intermediacy of an Anionic d10 Nickel Hydride. *J. Am. Chem. Soc.* **2017**, *139*, 14244.
(72) Vollmer, M. V.; Xie, J.; Lu, C. C. Stable Dihydrogen Complexes of Cobalt(−I) Suggest an Inverse trans-Influence of Lewis Acidic Group 13 Metalloligands. *J. Am. Chem. Soc.* **2017**, *139*, 6570.
(73) Culcu, G.; Iovan, D. A.; Krogman, J. P.; Wilding, M. J. T.; Bezpalko, M. W.; Foxman, B. M.; Thomas, C. M. Heterobimetallic Complexes Comprised of Nb and Fe: Isolation of a Coordinatively Unsaturated NbIII/Fe0 Bimetallic Complex Featuring a Nb≡Fe Triple Bond. *J. Am. Chem. Soc.* **2017**, *139*, 9627.
(74) Neese, F. Prediction and interpretation of the 57Fe isomer shift in Mössbauer spectra by density functional theory. *Inorg. Chim. Acta* **2002**, *337*, 181.
(75) Greenwood, N. N.; Gibb, T. C. *Mössbauer Spectroscopy*; Chapman and Hall Ltd: London, 1971.
(76) Gutlich, P.; Bill, E.; Trautwein, A. X. *Mössbauer Spectroscopy and Transition Metal Chemistry: Fundamentals and Applications*; Springer: Berlin, 2011.
(77) Anderson, J. S.; Cutsail, G. E.; Rittle, J.; Connor, B. A.; Gunderson, W. A.; Zhang, L.; Hoffman, B. M.; Peters, J. C. Characterization of an Fe≡N−NH2 Intermediate Relevant to Catalytic N2 Reduction to NH3. *J. Am. Chem. Soc.* **2015**, *137*, 7803.
(78) Lee, Y.; Mankad, N. P.; Peters, J. C. Triggering N2 uptake via redox-induced expulsion of coordinated NH3 and N2 silylation at trigonal bipyramidal iron. *Nat. Chem.* **2010**, *2*, 558.
(79) Ye, S.; Bill, E.; Neese, F. Electronic Structures of the [Fe(N2)(SiPiPr3)]+1/0/−1 Electron Transfer Series: A Counter-intuitive Correlation between Isomer Shifts and Oxidation States. *Inorg. Chem.* **2016**, *55*, 3468.
(80) Neese, F. Theoretical spectroscopy of model-nonheme [Fe(IV)OL5]2+ complexes in their lowest triplet and quintet states using multireference ab initio and density functional theory methods. *J. Inorg. Biochem.* **2006**, *100*, 716.
(81) Mondal, B.; Neese, F.; Bill, E.; Ye, S. Electronic Structure Contributions of Non-Heme Oxo-Iron(V) Complexes to the Reactivity. *J. Am. Chem. Soc.* **2018**, *140*, 9531.
(82) Tomson, N. C.; Williams, K. D.; Dai, X.; Sproules, S.; DeBeer, S.; Warren, T. H.; Wieghardt, K. Re-evaluating the Cu K pre-edge XAS transition in complexes with covalent metal−ligand interactions. *Chem. Sci.* **2015**, *6*, 2474.
(83) MacMillan, S. N.; Lancaster, K. M. X-ray Spectroscopic Interrogation of Transition-Metal-Mediated Homogeneous Catalysis: Primer and Case Studies. *ACS Catal.* **2017**, *7*, 1776.
(84) Walroth, R. C.; Lukens, J. T.; MacMillan, S. N.; Finkelstein, K. D.; Lancaster, K. M. Spectroscopic Evidence for a 3d10 Ground State Electronic Configuration and Ligand Field Inversion in [Cu(CF3)-4]1−. *J. Am. Chem. Soc.* **2016**, *138*, 1922.
(85) Agnew, D. W.; DiMucci, I. M.; Arroyave, A.; Gembicky, M.; Moore, C. E.; MacMillan, S. N.; Rheingold, A. L.; Lancaster, K. M.; Figueroa, J. S. Crystalline Coordination Networks of Zero-Valent Metal Centers: Formation of a 3-Dimensional Ni(0) Framework with m-Terphenyl Diisocyanides. *J. Am. Chem. Soc.* **2017**, *139*, 17257.
(86) Walroth, R. C.; Uebler, J. W. H.; Lancaster, K. M. Probing CuI in homogeneous catalysis using high-energy-resolution fluorescence-detected X-ray absorption spectroscopy. *Chem. Commun.* **2015**, *51*, 9864.
(87) Girolami, G. S.; Rauchfuss, T. B.; Angelici, R. J. *Synthesis and Technique in Inorganic Chemistry*, 3rd ed.; University Science Books: Sausalito, CA, 1999.
(88) Rudd, P. A.; Liu, S.; Gagliardi, L.; Young, V. G.; Lu, C. C. Metal−Alane Adducts with Zero-Valent Nickel, Cobalt, and Iron. *J. Am. Chem. Soc.* **2011**, *133*, 20724.
(89) Brookhart, M.; Grant, B.; Volpe, A. F. [(3,5-(CF3)2C6H3)4B]-[H(OEt2)2]+: a convenient reagent for generation and stabilization of cationic, highly electrophilic organometallic complexes. *Organo-metallics* **1992**, *11*, 3920.
(90) Blessing, R. An empirical correction for absorption anisotropy. *Acta Crystallogr., Sect. A: Found. Crystallogr.* **1995**, *51*, 33.
(91) Sheldrick, G. SHELXT - Integrated space-group and crystal-structure determination. *Acta Crystallogr., Sect. A: Found. Adv.* **2015**, *A71*, 3.
(92) Sheldrick, G. Crystal structure refinement with SHELXL. *Acta Crystallogr., Sect. C: Struct. Chem.* **2015**, *C71*, 3.
(93) Hubschle, C. B.; Sheldrick, G. M.; Dittrich, B. ShelXle: a Qt graphical user interface for SHELXL. *J. Appl. Crystallogr.* **2011**, *44*, 1281.
(94) Spek, A. Structure validation in chemical crystallography. *Acta Crystallogr., Sect. D: Biol. Crystallogr.* **2009**, *65*, 148.
(95) Webb, S. *SIXPACK; Stanford Synchrotron Lightsource*; Stanford Linear Accelerator Center, Stanford University: Stanford, CA, 2002.
(96) Neese, F. *ORCA - An ab initio, Density Functional and Semi-empirical Electronic Structure Package*, 4.0; Universität Bonn: Bonn, Germany, 2017.
(97) Hedegard, E. D.; Kongsted, J.; Sauer, S. P. A. Improving the calculation of electron paramagnetic resonance hyperfine coupling tensors for d-block metals. *Phys. Chem. Chem. Phys.* **2012**, *14*, 10669.
(98) Weigend, F.; Ahlrichs, R. Balanced basis sets of split valence, triple zeta valence and quadruple zeta valence quality for H to Rn: Design and assessment of accuracy. *Phys. Chem. Chem. Phys.* **2005**, *7*, 3297.
(99) Römelt, M.; Ye, S.; Neese, F. Calibration of Modern Density Functional Theory Methods for the Prediction of 57Fe Mössbauer Isomer Shifts: Meta-GGA and Double-Hybrid Functionals. *Inorg. Chem.* **2009**, *48*, 784.
(100) Neese, F. Quantum chemical calculations of spectroscopic properties of metalloproteins and model compounds: EPR and Mössbauer properties. *Curr. Opin. Chem. Biol.* **2003**, *7*, 125.
(101) Godbout, N.; Havlin, R.; Salzmann, R.; Debrunner, P. G.; Oldfield, E. Iron-57 NMR Chemical Shifts and Mössbauer Quadrupole Splittings in Metalloporphyrins, Ferrocytochrome c, and Myoglobins: A Density Functional Theory Investigation. *J. Phys. Chem. A* **1998**, *102*, 2342.
(102) Neese, F. Importance of Direct Spin−Spin Coupling and Spin-Flip Excitations for the Zero-Field Splittings of Transition Metal Complexes: A Case Study. *J. Am. Chem. Soc.* **2006**, *128*, 10213.
(103) Pipek, J.; Mezey, P. G. A fast intrinsic localization procedure applicable for ab initio and semiempirical linear combination of atomic orbital wave functions. *J. Chem. Phys.* **1989**, *90*, 4916.
(104) Neese, F. *ORCA - An ab initio, Density Functional and Semi-empirical Electronic Structure Package*, 3.03; Universität Bonn: Bonn, Germany, 2014.

DOI: 10.1021/acs.inorgchem.9b00442
Inorg. Chem. 2019, 58, 6199−6214

(105) Neese, F. The ORCA program system. *WIREs Comput. Mol. Sci.* **2012**, *2*, 73.
(106) Becke, A. D. Density-functional exchange-energy approximation with correct asymptotic behavior. *Phys. Rev. A: At., Mol., Opt. Phys.* **1988**, *38*, 3098.
(107) Perdew, J. P. Density-functional approximation for the correlation energy of the inhomogeneous electron gas. *Phys. Rev. B: Condens. Matter Mater. Phys.* **1986**, *33*, 8822.
(108) Lenthe, E. v.; Baerends, E. J.; Snijders, J. G. Relativistic regular two-component Hamiltonians. *J. Chem. Phys.* **1993**, *99*, 4597.
(109) van Lenthe, E.; Baerends, E. J.; Snijders, J. G. Relativistic total energy using regular approximations. *J. Chem. Phys.* **1994**, *101*, 9783.
(110) van Wüllen, C. Molecular density functional calculations in the regular relativistic approximation: Method, application to coinage metal diatomics, hydrides, fluorides and chlorides, and comparison with first-order relativistic calculations. *J. Chem. Phys.* **1998**, *109*, 392.
(111) Schäfer, A.; Horn, H.; Ahlrichs, R. Fully optimized contracted Gaussian basis sets for atoms Li to Kr. *J. Chem. Phys.* **1992**, *97*, 2571.
(112) Schäfer, A.; Huber, C.; Ahlrichs, R. Fully optimized contracted Gaussian basis sets of triple zeta valence quality for atoms Li to Kr. *J. Chem. Phys.* **1994**, *100*, 5829.
(113) Klamt, A.; Schüürmann, G. COSMO: a new approach to dielectric screening in solvents with explicit expressions for the screening energy and its gradient. *J. Chem. Soc., Perkin Trans. 2* **1993**, 799.
(114) Stephens, P. J.; Devlin, F. J.; Chabalowski, C. F.; Frisch, M. J. Ab Initio Calculation of Vibrational Absorption and Circular Dichroism Spectra Using Density Functional Force Fields. *J. Phys. Chem.* **1994**, *98*, 11623.
(115) Neese, F.; Wennmohs, F.; Hansen, A.; Becker, U. Efficient, approximate and parallel Hartree−Fock and hybrid DFT calculations. A 'chain-of-spheres' algorithm for the Hartree−Fock exchange. *Chem. Phys.* **2009**, *356*, 98.
(116) Broere, D. L. J.; Mercado, B. Q.; Lukens, J. T.; Vilbert, A. C.; Banerjee, G.; Lant, H. M. C.; Lee, S. H.; Bill, E.; Sproules, S.; Lancaster, K. M.; Holland, P. L. Reversible Ligand-Centered Reduction in Low-Coordinate Iron Formazanate Complexes. *Chem. - Eur. J.* **2018**, *24*, 9417.
(117) Wilding, M. J. T.; Iovan, D. A.; Wrobel, A. T.; Lukens, J. T.; MacMillan, S. N.; Lancaster, K. M.; Betley, T. A. Direct Comparison of C−H Bond Amination Efficacy through Manipulation of Nitrogen-Valence Centered Redox: Imido versus Iminyl. *J. Am. Chem. Soc.* **2017**, *139*, 14757.

DOI: 10.1021/acs.inorgchem.9b00442
Inorg. Chem. 2019, 58, 6199−6214